A Simple Model for Tropical Convective Cloud Shield Area Time Tendencies Informed by Geostationary IR, GPM, and Aqua/AIRS Satellite Data

Gregory Elsaesser[1,1], Remy Roca[2,2], thomas fiolleau[3,3], Anthony D. Del Genio[4,4], and Jingbo Wu[5,5]

[1]Columbia University APAM/NASA GISS
[2]Laboratoire d'Etudes Géophysiques et d'Océanographie Spatiale, Toulouse, France
[3]Laboratoire d'études en Géophysiques et Océanographie Spatiales - LEGOS (CNRS)
[4]National Aeronautics and Space Administration (NASA)
[5]Columbia University

November 30, 2022

Abstract

Deep convective system maximum areal extent is driven by the stratiform anvil area since system convective area fractions are much less than unity when systems reach peak size. It is important to understand the processes that drive system size given the impact large systems have on rainfall and since anvils may strongly impact high cloud feedbacks. Using satellite diabatic heating and convective-stratiform information mapped to convective systems, composite analyses suggest that system maximum sizes occur at the temporal mid-point of system lifecycles with both maximum size and duration correlating with peak heating above the melting level. However, variations in system growth rates exist, with the overall smooth composites emerging as the average of highly variable system trajectories. Thus, this study focuses on understanding convective system growth rates on short (30-minute) timescales via development of a simple analytical source - sink model that predicts system area changes. Growth occurs when detrained convective mass (inferred from the vertical gradient of diabatic heating and temperature lapse rates) and/or generation of convective area exceeds a sink term whose magnitude is proportional to the current cloud shield size. The model works well for systems over land and ocean, and for systems characterized by varying degrees of convective organization and duration (1.5 - 35 hr, with correlations often >0.8 across lifetime bins). The model may serve as a useful foundation for improved understanding of processes driving changes in tropics-wide convective system cloud shields, and further supports conceptual development and evaluation of prognostic climate model stratiform anvil area parameterizations.

A Simple Model for Tropical Convective Cloud Shield Area Growth and Decay Rates Informed by Geostationary IR, GPM, and Aqua/AIRS Satellite Data

Gregory S. Elsaesser[1,2], Rémy Roca[3], Thomas Fiolleau[3],

Anthony D. Del Genio[2,†], Jingbo Wu[1,2]

[1]*Department of Applied Physics and Mathematics, Columbia University, New York, New York, USA*

[2]*NASA Goddard Institute for Space Studies, 2880 Broadway, New York, New York, USA*

[2]*Laboratoire d'Etudes en Géophysique et Océanographie Spatiales, Observatoire Midi-Pyrénées, Toulouse, France*

Corresponding Author: Gregory S. Elsaesser, Department of Applied Physics and Applied Mathematics, Columbia University/NASA Goddard Institute for Space Studies, 2880 Broadway, New York, New York, Tel: (212) 678-5596, gregory.elsaesser@columbia.edu

†*Now retired*

Key Points:

- A simple analytical model for cloud area growth and decay rates is developed, with a source term driven by convective cell diabatic heating.
- The model works equally well for convective systems of varying duration and degrees of convective organization over both land and ocean.
- The model suggests that a convective area fraction of ~ 0.2 is needed for stratiform cloud area maintenance.

Abstract

Deep convective system maximum areal extent is driven by the stratiform anvil area since convective area fractions are much less than unity when systems reach peak size. It is important to understand the processes that drive system size given the impact large systems have on rainfall and that of anvils on high cloud feedbacks. Using satellite diabatic heating and convective-stratiform information mapped to convective systems, composite analyses suggest that system maximum sizes occur at the temporal mid-point of system lifecycles with both maximum size and duration correlating with peak heating above the melting level. However, variations in system growth rates exist, with the overall smooth composites emerging as the average of highly variable system trajectories. Thus, this study focuses on understanding convective system growth rates on short (30-minute) timescales via development of a simple analytical source – sink model that predicts system area changes. Growth occurs when detrained convective mass (inferred from the vertical gradient of diabatic heating and temperature lapse rates) and/or generation of convective area exceeds a sink term whose magnitude is proportional to the current cloud shield size. The model works well for systems over land and ocean, and for systems characterized by varying degrees of convective organization and duration (1.5–35 hr, with correlations often >0.8 across lifetime bins). The model may serve as a useful foundation for improved understanding of processes driving changes in tropics-wide convective system cloud shields, and further supports conceptual development and evaluation of prognostic climate model stratiform anvil area parameterizations.

1 Introduction

Mesoscale convective systems (MCSs) are the dominant sources of rainfall in the tropics (Tao and Moncrieff, 2009; Roca et al., 2014; Moncrieff, 2019). MCS cloud shields comprise convective regions whose spatial aggregation may be quantified via "organization metrics" (Parker and Johnson, 2000; Tobin et al., 2012; Tobin et al., 2013; Holloway et al., 2017; Retsch et al., 2020) such that increased organization may be associated with larger cloud shields, longer lifetimes and substantial rainfall accumulation (Liu et al., 2008; Liu, 2011; Roca and Fiolleau, 2020; Schiro et al., 2020). High resolution model simulations over domains populated by MCSs are frequent sources for deriving MCS radiation, cloud, and rainfall lifecycle evolutions (Hagos et al., 2013; Feng et al., 2018; Feng et al., 2021). Observational composite MCS evolutions can be derived by mapping orbital-level satellite-estimated radiation, cloud, rainfall, and environment characteristics to the life stages of IR-tracked MCSs (as in Machado et al., 1998; Machado and Laurent, 2004; Futyan and Del Genio, 2007; Feng et al., 2012; Fiolleau and Roca, 2013b; Bouniol et al., 2016; Vant-Hull et al., 2016; Roca et al., 2017; Roca et al., 2020), or by mapping in situ environmental data to scanning radar-identified MCSs (e.g., Wang et al., 2019; Wang et al., 2020). One such compositing analysis has revealed that MCSs over the open ocean cool the sea surface temperature (SST), a signature that lasts for days (Duncan et al., 2014) and is likely to affect the subsequent development of convection.

MCS convective regions are characterized by diabatic heating profiles whose magnitudes are positive throughout most of the troposphere, though spread over a smaller area, while the extensive moderately raining stratiform anvil region is characterized by widespread positive heating that peaks above the melting level with diabatic cooling below (Elsaesser et al., 2010; Liu et al., 2015; Feng et al., 2018) attributed to melting snow and precipitation evaporation below cloud base. The heating profiles combine to yield top-heavy system-average heating profiles (Houze, 1989; Houze, 2004; Elsaesser et al., 2010; Hannah et al., 2016; Feng et al., 2018) that tightly couple to large-scale tropical circulations (Hartmann et al., 1984; Schumacher et al., 2004; Inoue and Back, 2015). Ice particles, laterally detrained by convection, contribute to the growth of the raining stratiform anvil region. Both the rate at which ice particles are detrained and particle fall speeds impact the areal extent of the stratiform area. General circulation models (GCMs) are typically crude in their parameterization of detrained ice (Elsaesser et al., 2017; Lin et al., 2021), and thus, have trouble simulating the growth of stratiform area, let alone parameterizing MCSs (Moncrieff et al., 2017; Moncrieff, 2019).

However, GCMs may still simulate relatively unbiased global rainfall and diabatic heating climatologies in the absence of successful MCS simulation, given that GCM tuning procedures focus on improving mean states (Mauritsen et al., 2012; Schmidt et al., 2017) with little or no penalty for discrepancies cancelling at the cloud-system scale. Structural parameterization errors are rarely tuned away, and they manifest themselves in biased regional rainfall rate distributions, large-scale modes of tropical variability, and cloud feedbacks. Accurate simulation of cloud feedbacks is important, and since tropical high cloud fields are largely the product of convective detrainment (Bony et al., 2016; Seeley et al., 2019) and residual MCS cloud shields, the contribution of tropical high clouds to total cloud feedbacks may be quite related to how well MCSs are simulated in the parent GCM. These complicated modes of convection are certainly one reason moist convection is a large source of uncertainty in our ability to project climate change (e.g., Bony et al., 2015; Schneider et al., 2017). Improved projections of regional rainfall distributions, more accurate simulation of cloud feedbacks and equilibrium climate sensitivity, and improved understanding of MCS trends emerging from high resolution simulations (Prein et al., 2017) and observations (Tan et al., 2015) requires continued work on determining the dominant drivers of system evolutions and their extensive cloud shields.

To this end, we perform new MCS observational analyses that build on previous MCS lifecycle compositing studies (section 3.1) and then turn our attention to the often-variable MCS cloud shield growth and decay rates, with a goal of understanding how these growth and decay rates relate to diabatic heating profiles (section 3.2 and 3.3). Since the vertical derivative of diabatic heating in convection ties to mass divergence, and mass divergence influences cloud shield changes, we contribute to research aiming to determine the factors that drive changes in stratiform anvils (e.g., Seeley et al., 2019; Hagos et al., 2020) with a focus on the development of a simple analytical source-sink model for cloud shield area changes informed by satellite data aggregated over the global tropics. These analyses will serve as a conceptual framework for continued development of organized convection parameterization in the GISS model, and can inform GCM convective parameterization development more broadly.

2 Data Sources

2.1 Satellite Observational Products

Aqua AIRS/AMSU (Chahine et al., 2006) version 6 data for temperature (available for the entire tropospheric column) and water vapor (for pressure levels > 300 hPa), along with Microwave Limb Sounder (MLS; Waters et al., 2006) version 3 data for water vapor profiles at pressure levels < 300 hPa, serve as the observed thermodynamic data sources in this work. Convective and stratiform pixel identification (Level 2 data) derived from the Global Precipitation Measurement (GPM; Skofronick-Jackson et al., 2017) mission Dual-frequency Precipitation Radar (DPR; Iguchi et al., 2012) product, rainfall from the Level 2 combined (DPR+GMI; Grecu et al., 2016) product, and diabatic heating (often denoted as Q_1-Q_R hereafter, or a heating term defined here that includes all components except horizontal eddy flux convergence and radiative heating) from the Level 2 Convective-Stratiform Heating (CSH; Lang and Tao, 2018) and Spectral Latent Heating (SLH; Shige et al., 2009) products serve as the observed convective and stratiform precipitation and heating sources. AIRS/MLS and GPM orbital-level data are mapped to the MCS cloud shield provided by the TOOCAN convective system tracking algorithm (Fiolleau and Roca, 2013a,b). For compositing results shown in section 3, at least 1/3 of the system cloud shield must be sampled by GPM in order for measurements to be included in averaging. In order for GPM overpass data to be used in the analytical model development and associated coefficient estimation, at least 2/3 of the cloud shield must be sampled by GPM. Sensitivity of some results to this coverage threshold is discussed in section 3.4.

2.2 TOOCAN Convective System Tracking Database

The Tracking Of Organized Convection Algorithm through a 3-D segmentatioN (TOOCAN; Fiolleau and Roca, 2013a) methodology, applied to infrared (IR) brightness temperature (BT) data observed from a fleet of geostationary platforms, serve as our source of MCSs (defined here as precipitating cloud systems, of spatial scale O(100km), that occur in connection with thunderstorms). The TOOCAN approach aims to retain the spatial association between the convective region of MCSs and their attendant stratiform anvil component. The algorithm operates within a space-time volume of IR images, and applies a 3-D image processing technique to decompose the cold cloud shield (delineated by a 235K threshold) in the spatio-temporal domain into component MCSs. The algorithm is based on an iterative process of detection and dilation of convective seeds in the spatio-temporal domain. Individual convective seeds are first detected in 3D by applying a given BT threshold in the volume of IR images. Convective seeds with a minimum lifetime duration of 1.5h and exceeding 625km^2 per frame are extracted. Each detected convective seed is spread in the spatiotemporal domain until it reaches the intermediate cold cloud shield boundaries identified at a 5K warmer BT threshold. This step consists in adding edge pixels belonging to the intermediate cold cloud shield to all already detected seeds. The dilation of the convective seeds is performed by using a 10-connected spatiotemporal neighborhood (8-connected spatial neighborhood and 2-connected temporal neighborhood) to favor spatial dilation rather than the temporal dilation. Note that the pixel aggregation process is constrained by a BT difference between the edge and current pixel, which has to be greater than -1K to minimize the effects of local minima. The iterative process starts with a detection of the convective seeds set at a 190K BT threshold, works with a 5K detection step, and is stopped when the 235K threshold is reached. The TOOCAN algorithm is unique in that it avoids the convective system split and merge artifacts associated with traditional tracking algorithms, thus enabling MCSs and their attendant cloud shield sizes to be accurately tracked along their entire life cycles from early initiation stages to the later dissipation stages.

For this study, IR from MSG-3, GOES-13 and 15, METEOSAT-7, and MTSAT-2 are used, and MCSs within the tropical belt (30°S-30°N) from Mar – Dec 2014 are tracked. The IR sensors hosted on geostationary platforms exhibit instrument and engineering differences (e.g., different spatial and temporal resolutions, observation frequencies, spectral responses, calibrations). All IR data have been remapped to a common 0.04° equal angle grid while the temporal resolution has been unified to 30 minutes across all geostationary platforms to avoid an over-segmentation of the MCSs detected (Fiolleau et al., 2020). Additionally, there has been an effort to inter-calibrate IR data across sensors prior to ingestion into TOOCAN. The scanning schedule of MTSAT-2 does not provide a half-hourly sampling of the Southern Hemisphere region at the time of this analysis; therefore, this region is not considered in this study. Additionally, we only analyze convective systems if they are separated from tropical cyclones, mid-latitude cyclones, and fronts. The IBTrACS database (Knapp et al., 2010) and mid-latitude system databases (Naud et al., 2010; Naud et al., 2016) serve as the sources for selecting which MCSs to remove, with roughly 40,000 GPM-intersected systems remaining for analyses.

3 Results

3.1 Composite Convective System Diabatic Heating Lifecycles and System Durations

Several snapshots of convective systems are shown in Fig. 1. These examples suggest system sizes are predominantly driven by changing stratiform areal extent, and to a much lesser extent,

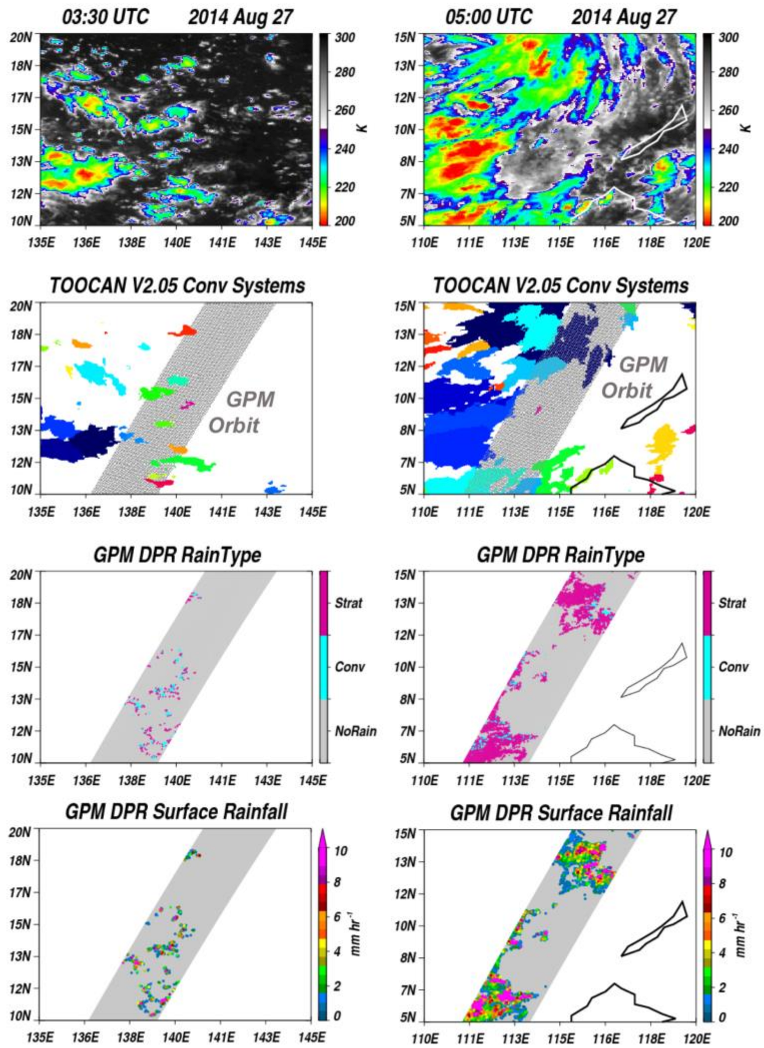

Figure 1. (Left) From top to bottom, a snapshot (03:30 UTC, 2014 Aug 27) of IR brightness temperatures, observed convective systems (distinct systems are color-coded), GPM rain classification (stratiform, convective, no-surface-rain) , and GPM surface rainfall. (Right) as to the left, but for a different geographic location and time (05:00 UTC).

varying convective extent. Close visual inspection of Fig. 1 shows that convective areas may be clustered on the edges of system shields or dispersed throughout, similar to Yuter and Houze (1998) and Fridlind et al. (2012), while anvil cloud shields extend beyond raining stratiform regions. For systems of varying durations, Fig. 2 shows the composite Q_1-Q_R , convective area fractions and system sizes as a function of system lifecycle stage. Most convective systems are irregularly shaped, and the "system size" computed (and often referred to hereafter) is the diameter of a circle whose area is equivalent to the TOOCAN-identified cloud shield area. At and shortly after initiation (i.e., hr-0 life stage), convective area fractions and system sizes are similar regardless of system duration

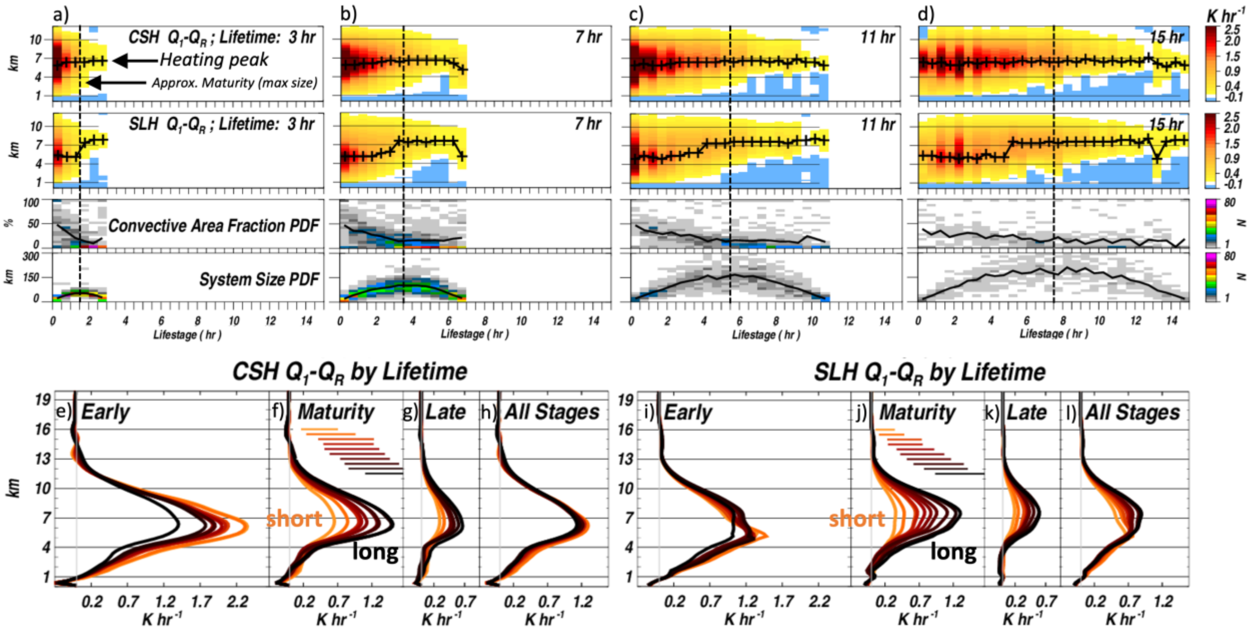

Figure 2. (a – d) For convective systems of different durations (3-, 7-, 11- and 15-hr), the composite CSH and SLH Q_1-Q_R, convective area fractions, and system sizes (distributions are shown for the latter two variables to illustrate variability; solid lines denote average) as a function of system life stage. (e - l) The composite CSH and SLH Q_1-Q_R averaged over the early (initiation – 0.45), mature (0.45 – 0.55) and late (0.55 – termination) stages of the system lifecycles, color coded so that longer-lived systems are shaded darker (duration bins 3-, 5-, 7-, 9-, 11-, 13-, 15-, 19-, 25-, and 31-hr, respectively). For the mature-stage panels (f, j), horizontal lines denote the 1σ range in Q_1-Q_R at 7 km (also color coded by same duration bins).

(Figs. 2a-d, third and fourth row), with SLH Q_1-Q_R being of comparable magnitude for all system durations (Fig. 2i), while CSH Q_1-Q_R is weaker in longer-lived vs shorter-lived systems (Fig. 2e).

The SLH product is developed using diabatic heating from Tropical Ocean Global Atmosphere-Coupled Ocean-Atmosphere Response Experient (TOGA COARE) field campaign simulations while the CSH product is developed using 10 tropical land and ocean field campaign simulations, as discussed in Tao et al. (2016), so it is possible that similarity in SLH profiles during early stage convection (Fig. 2i) may reflect the use of Q_1-Q_R informed by one convection regime. TOGA COARE convection was also characterized by larger stratiform rainfall fractions (Tao et al., 2016) and further exhibited a very clear shallow – deep – stratiform transition (Lin et al., 2004; Kiladis et al. 2005). This may explain why, relative to CSH, the altitude of peak SLH Q_1-Q_R (Figs. 2a-d, second rows) shifts upward as MCS life stages advance and why SLH Q_1-Q_R is more top heavy relative to CSH in overall composites (compare Figs. 2j-l to Figs. 2f-h).

For the purposes of conveniently quantifying Q_1-Q_R at system peak, we define a "maturity" metric as the time at which a system reaches maximum size. At maturity, aside from longer-lived systems achieving a larger-size (evident from the system size PDFs), longer-lived systems are characterized by increased maximum Q_1-Q_R (typically near 7-km; Figs. 2f, j), with the 1σ range in peak heating for each system duration suggesting this is a robust result. Secondly, maturity marks the onset of near negligible Q_1-Q_R heating that begins in the boundary layer but gradually extends vertically to the melting level (~5-km) as the system ages and dissipates (Figs. 2f-g, and Figs. 2j-k). Since convective area fractions reach their minimum near maturity and are nearly invariant thereafter (Figs. 2a-d, third rows), this implies that system vertical heating structures and convective-stratiform fractions do not uniquely map to each other. Furthermore, it is very clear that convective area fractions do not map uniquely to duration, either.

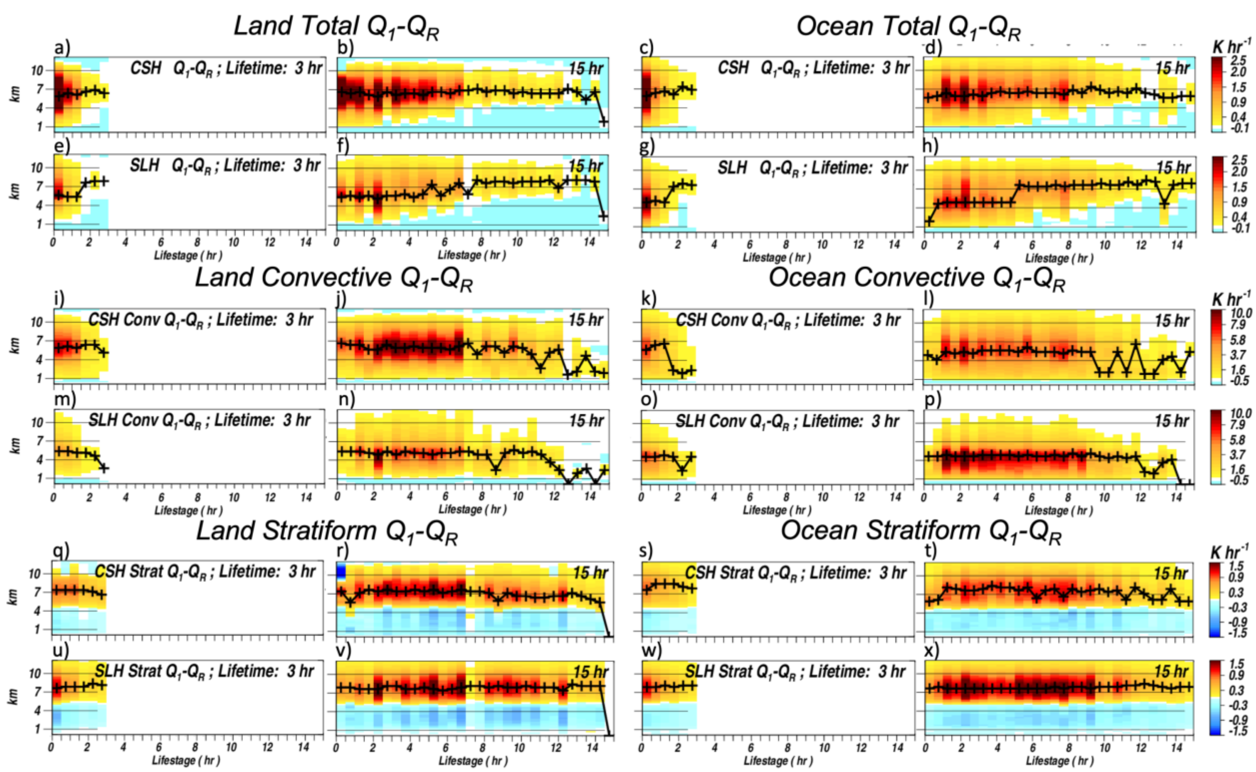

Figure 3. For convective systems of 3 and 15-hr duration (over land and ocean separately), the CSH and SLH Q_1-Q_R as a function of system life stage (a – h). Composites are also partitioned into convective region-average (i – p) and stratiform region-average Q_1-Q_R (q – x) components. As in Fig. 2a-d, the plus symbols in each panel denote the altitude of peak heating as a function of life stage. *Note the difference in Q_1-Q_R magnitude range and color scales across each panel, and relative to Fig. 2 ranges.*

Fig. 3 shows Q_1-Q_R averaged over the convective and stratiform portions of the cloud shield (in addition to system-average Q_1-Q_R composites in the top rows [Figs. 3a-g], as in Fig. 2). Fig. 3 suggests that CSH convective Q_1-Q_R is larger over land (Figs. 3i-j) than ocean (Figs. 3k-l), consistent with studies documenting that convection over land is more intense (e.g., Zipser and Lemone, 1980; Lucas et al., 1994; Takahashi et al., 2017; Takahashi et al., 2021). SLH shows the opposite behavior in convective Q_1-Q_R (Figs. 3m-p), which again may be reflective of CSH retrievals being informed by both land and ocean field campaigns, whereas SLH is informed solely by the TOGA COARE oceanic convection environment. Both CSH and SLH yield similar stratiform heating composites (Figs. 3q-x), perhaps a result of less innate variability in stratiform rain vertical structures (Houze, 1989; Schumacher and Houze, 2006) thus implying less dependence on CSH or SLH look-up tables and algorithms. Since convective heating begins rapidly dissipating shortly before mid-lifecycle stages (Figs. 3i-p), the weaker convective heating in the lower troposphere is eventually overwhelmed by the nearly lifecycle-independent stratiform anvil cooling signature (Figs. 3q-x) which results in system-average cooling below the melting level later in later life stages (Fig. 2 and Figs. 3a-h). Despite the stratiform heating not varying substantially as a given system progresses, it varies from one system duration to another, with longer-lived systems exhibiting slightly larger amplitude stratiform heating-cooling signatures (Figs. 3q-x).

Are the composites shown in Figs. 2 and 3 representative of most convective systems? Focusing on the middle lifecycle stages of convection systems, one interpretation of the system size PDF variability (Figs. 2a-d, last row) is that systems hobble along, growing and decaying randomly, with the time of maximum system size deviating from the temporal mid-point but with system longevity mapping strongly to maximum size. Quantitatively, this would be reflected in a smaller correlation between individual system size temporal evolutions and the composite system size evolutions shown in Fig. 2. An alternate interpretation is that there is simply variability in the maximum system size for a system of a given lifetime (with the maximum occurring at the temporal mid-point), but with consistent increases in system size from initiation up to that point, and consistent decay toward termination, thus implying high correlation between the composite evolution and individual system evolutions. Fig. 4 sheds light on these questions. There is a clear relationship between system size and lifetime (Fig. 4a; quantitatively, the percent variance explained between maximum area and lifetime is > 50%), similar to Feng et al. (2012) and shown in Roca et al. (2017). There is, however, little relationship between growth at the early stages of convection and lifetime

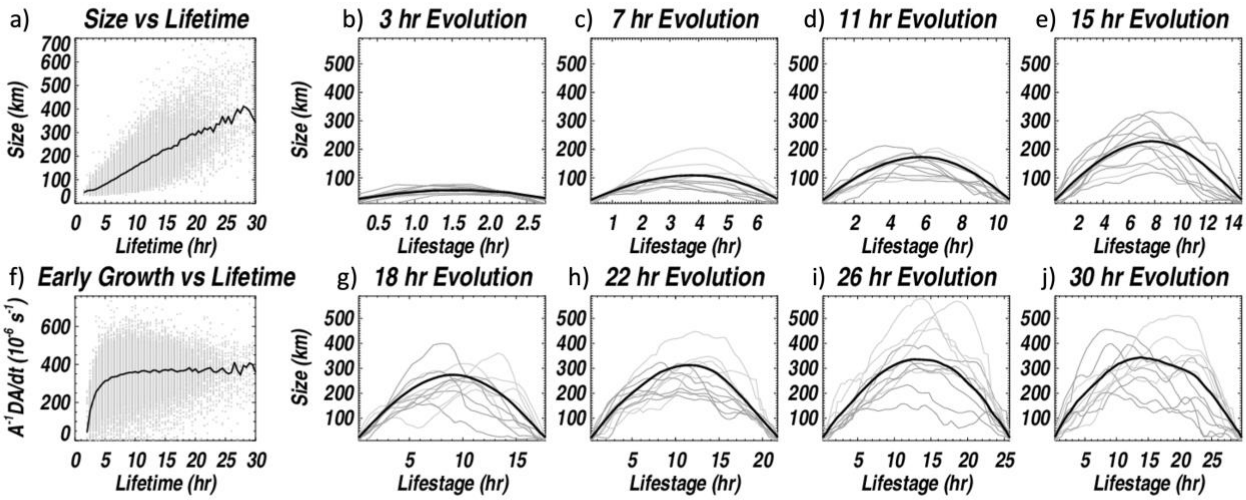

Figure 4. (a) Convective system maximum size as a function of lifetime, with the composite relationship overplotted as a solid line; (f) Early growth scatterplot (and solid line composite) as a function of lifetime. The remaining 8 panels show the composite system size evolution as a function of time for convective systems of varying lifetimes (solid black), with a random selection of 10 individual system evolutions overplotted for each lifetime panel (thin grey lines).

across durations (Fig. 4f; also similar to Feng et al., 2012), somewhat in contrast to Machado and Laurent (2004), though that study was limited to one regime and mostly focused on shorter-lived system relationships. This suggests that there is variability in the system size temporal evolution. A comparison of composite system evolutions and randomly-selected individual systems show that systems take different evolution trajectories (e.g., Figs. 4b-e, and g-j). While many systems reach their maximum at the temporal middle point of their lifecycle (as in Roca et al. (2017) and Feng et al. (2019)), the evolutions shown here suggest that some may grow slowly, then more quickly, or vice versa.

How should we understand the system trajectories? Regardless of whether cloud shield sizes systematically increase toward a maximum and decrease after, or whether the path toward and beyond a maximum is characterized by many ups and downs, both trajectories suggest substantial variability in actual cloud shield growth rates. Thus, we consider individual system trajectories as an accumulation of substantially varying instantaneous growth and decay sequences and aim to better understand the instantaneous growth rates themselves, assuming that the overall smooth composites emerge as the average of all individual trajectories.

3.2 Development of source – sink model for convective system cloud shield areas.

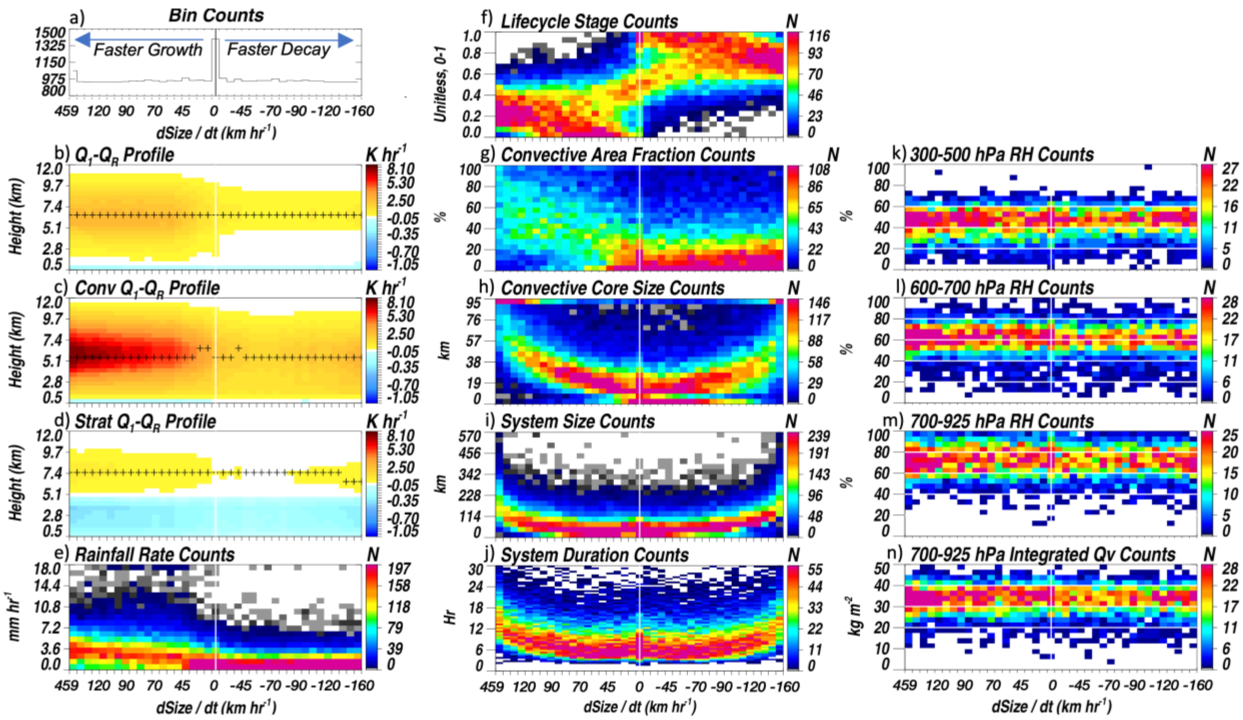

Figure 5. (left column) From top to bottom, bin counts, composite total, CSH convective and stratiform Q_1-Q_R profiles and surface rainfall rate histograms as a function of the cloud shield size rate of change. Total heating is averaged over the raining region, convective and stratiform heating profiles are averaged over their respective cloud type areas as in Fig. 3, and rainfall rate is a system average. (middle column) Various parameter histograms plotted as a function of the cloud shield size rate of change. (right column) As in the center column, but for Aqua/AIRS retrieved relative humidity (RH) for three different levels, and integrated water vapor in the lower troposphere. As in Fig. 2a-d, the plus symbols in the heating panels denote the altitude of peak heating. The white vertical lines denote the zero cloud shield size rate of change bin, and horizontal white lines in right column are added to aid in visual interpretation.

Fig. 5 shows MCS characteristics as a function of system growth and decay rates. Cloud shield size time tendency bin widths are objectively chosen so that approximately the same number of samples occur within each bin (symmetric about zero). It is clear that an asymmetry in growth and decay rates exists in Fig. 5a with the largest growth rate magnitudes exceeding the largest decay rate magnitudes. Because decay rates on average are much slower, a short-lived sequence of rapid growth has a large potential to extend the duration of a system cloud shield area. While difficult to infer from the composite lifecycle perspectives (Figs. 2 and 3), Fig. 5 suggests that growth in convective systems is strongly proportional to the convective area fraction (Fig. 5g) and convective area Q_1-Q_R (or the vertical derivative of Q_1-Q_R above the melting level, since Q_1-Q_R tends toward zero above 15 km). For simplicity, only CSH Q_1-Q_R is shown in Fig. 5; a repeat of analyses using the SLH product yields similar interpretations. Is the state of convective cores themselves (Q_1-Q_R structure, and size) during growth the dominant factor in growth rates and ultimately, duration? Growth and decay broadly map to the first and last half of the lifecycles, respectively, but, consistent with the individual system evolutions in Fig. 4, there is no one-to-one correspondence with life stage.

Nearly all of the largest system-average rainfall rates are found during system growth stages (Fig. 5e). Since average rainfall peaks early in lifecycle composites (Fiolleau and Roca, 2013b; Feng et al., 2019; Feng et al., 2021) and longer-lived systems contribute more to extreme precipitation (Feng et al., 2018; Roca and Fiolleau, 2020), this may imply that rainfall extremes specifically occur during growth periods of the early lifecycle stages. There is little relationship between growth and decay rates, life stage (Fig. 5f), and moisture (Figs. 5k-n). PDFs of heating, sizes and durations, if sorted according to the relative humidity (RH) at any level, also show little variation, so the interpretation is consistent. It is worth noting that all of these RH values are much wetter than the tropics-wide average implying that the existence of tropical MCSs (and their expansive raining cloud shields) depends on humid conditions though actual system growth rates do not. Growth and decay rates are inevitably tied to system duration (Fig. 5j), and a lack of relationship with moisture is consistent with the weak role that saturation fraction plays in driving the specific onset time and duration of heavy rainfall (Elsaesser et al., 2013).

What is the cause of system cloud shield decay? It is less surprising that no relationship between growth rates and moisture exists, particularly if cold pool – local environment interactions (e.g., storm relative shear), gravity waves, sea breezes, or other small-scale factors are drivers of upscale growth, though some studies suggest a moistening driven by previous convection (Rapp et al., 2009; Mapes and Neale, 2011) may favor subsequent convection (which, in a Lagrangian tracking sense, implies > 0 growth rates). For the decay portion of the spectrum, when convection is absent or weak, if systems are not running into a drier environment, how do we determine why systems decay? Among the clear signals that do manifest during decay: convective area is often absent (Fig. 5h), or, if present, convective area fractions are often small (Fig. 5g), and decay rates themselves are proportional to system size (Fig. 5i).

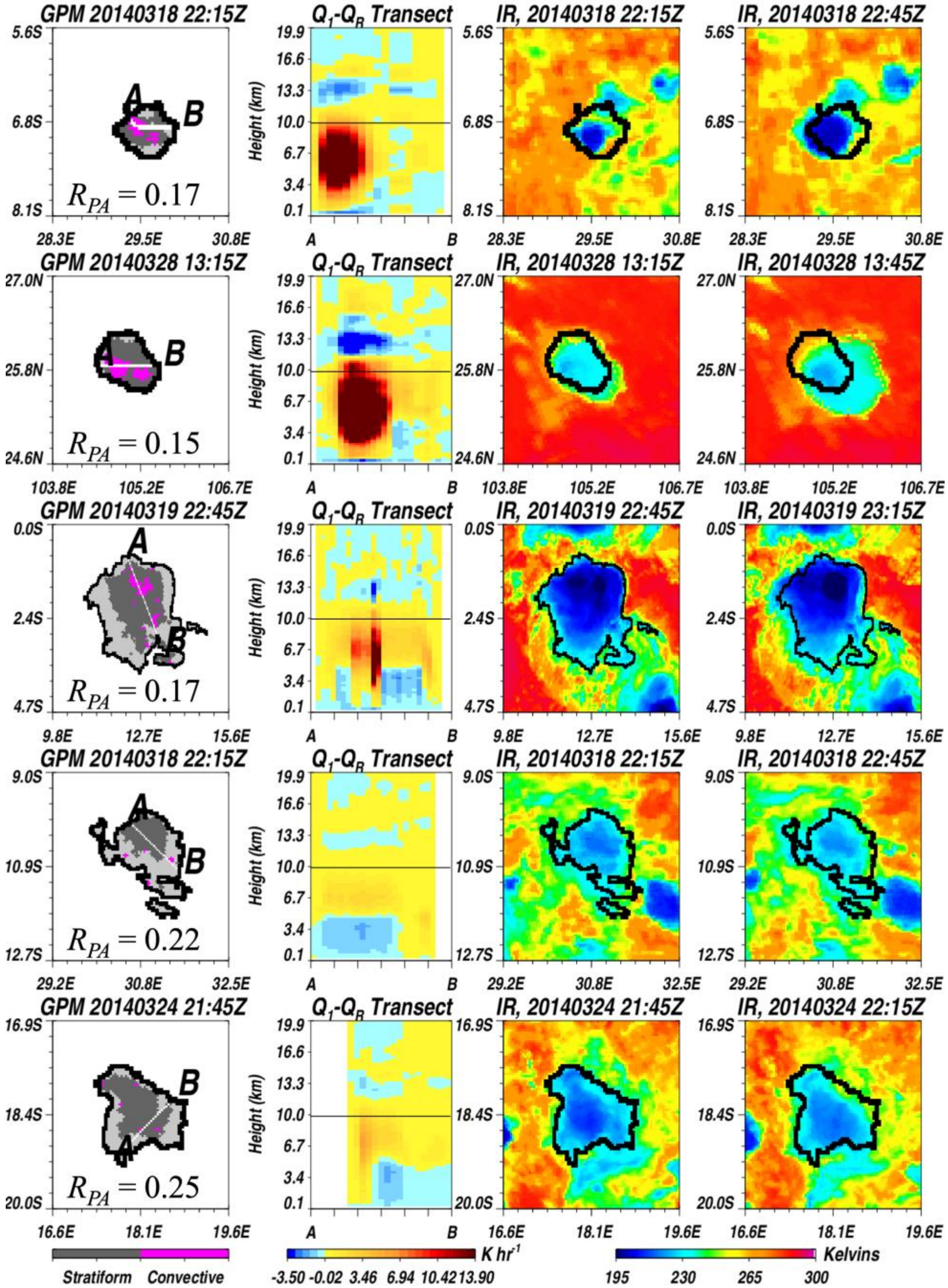

Figure 6. For different convective system examples (rows) over land, from left to right: co-located GPM convective-stratiform field (non-raining scene shaded in light grey, with the corresponding R_{PA} [see text and Fig. 7] shown for each system); CSH Q_1-Q_R profiles along the A – B transect; IR brightness temperature field at the time of the GPM overpass; and, IR brightness temperature field 30 minutes after the GPM overpass. The black horizontal line near 10 km in the A – B transect panels denote the approximate 235 – 240 Kelvin temperature level (approx. threshold for cloud shield distinction). The solid black circular line in all panels of the 1st, 3rd and 4th columns does not change, and is used for visually gauging the changing IR cloud shield size.

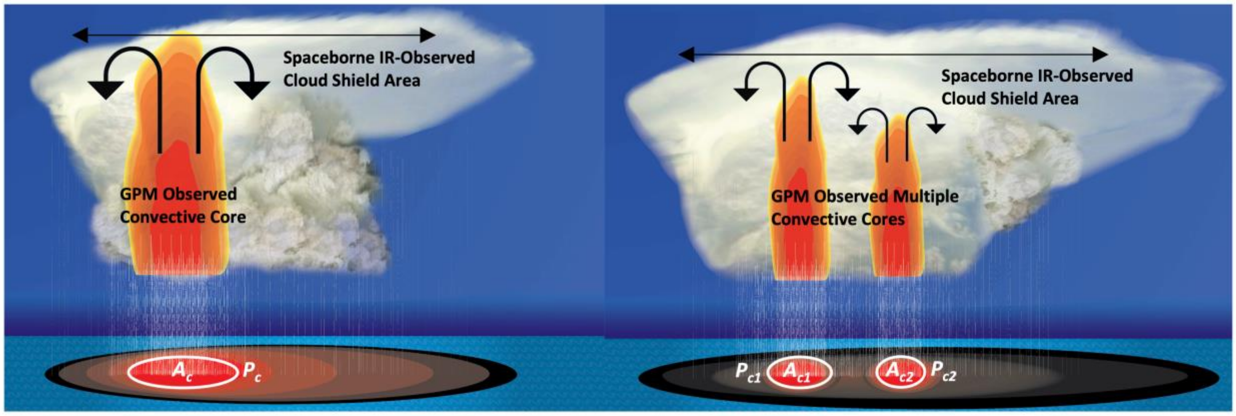

Figure 7. Schematic of distributed convective cores in tracked convective systems, where to the left, convection is aggregated into one cell of area A_c and cell perimeter P_c, and to the right, the same total convective area is observed, but is split across two convective cells of differing areas (A_{c1}, A_{c2}) and cell perimeters (P_{c1}, P_{c2}). Since $P_{c1} + P_{c2} > P_c$, the ratio of the sum of convective cell perimeters to total convective area (i.e., referred to as R_{PA} in the text) increases as convective aggregation decreases (i.e., R_{PA} is larger for less convectively-aggregated system in right panel).

If system growth rates are related to the vertical derivative of convective Q_1-Q_R, then we can apply the concept of vertical convective mass flux convergence as a source for cloud shield area time tendencies (and thus, the magnitudes of growth rates), terms quantifiable using data from the current combination of satellite sensors in orbit. Fig. 6 shows two cases of rapidly growing cloud shields (top two rows) for systems characterized by strongly-heating convective regions and a third system, characterized by weaker convective Q_1-Q_R, whose shield is growing more slowly. The bottom two rows of Fig. 6 are examples of systems whose cloud shields are decaying. The decaying systems have little convection observed by GPM, and there is a sense that shield decay is slow and somewhat diffuse. These examples reflect the statistics shown in Fig. 5: growth can be rapid, and is likely associated with convection and a large vertical derivative of convective Q_1-Q_R. Decay is slower and occurs with a weakened convection area, or in many cases, occurs in the absence of a convective source, while being proportional to system size. Other interesting features in Fig. 6 include differences in the spatial aggregation of convective cells. For example, in the second row, convective area is very aggregated, while in the third row, the total convective area is nearly equivalent, though the area is now dispersed across numerous cells spanning the cloud shield. Cell aggregation can be quantified by computing the ratio of the sum of convective perimeters to total convective area (referred to as R_{PA} hereafter). R_{PA} is provided for each system example in the first column of Fig. 6.

The sum of convective perimeters was computed by adding up all edge 4-km GPM DPR pixels surrounding the GPM identified convective regions of the tracked convective system. As R_{PA} increases, convection becomes dispersed, i.e., more cells for a given area (see Fig.7 schematic for an illustration of systems with the same total cell area but different R_{PA}). How does R_{PA} relate to system growth rates?

Supported by the results thus far, and building on the conceptual MCS sustainability ideas previously proposed (e.g., Yuter and Houze, 1998; Schumacher and Houze, 2007; Futyan and Del Genio, 2007), an analytical model of the system cloud shield time tendency, with source terms driven by a temporal generation-of-convective-area term, vertical convective and stratiform mass flux convergence terms forcing lateral cloud shield expansion, and a sink term proportional to the cloud area, can be structured as follows:

$$\frac{dA}{dt} \approx A_{c,\mathrm{SRC}} - \frac{1}{\rho}\frac{dM_c}{dz} - \frac{1}{\rho}\frac{dM_s}{dz} - \frac{A}{\tau}, \tag{1}$$

where A is the cloud shield area, A_c is the convective area (with the subscript 'SRC' indicating this term represents the temporal generation of new convective area), M_c is the convective mass flux, M_s is the stratiform mass flux, ρ is the atmospheric density, and τ is a cloud shield area decay timescale. For comparison purposes, after moving the first term on the rhs of Eq. (1) to the lhs, the equation becomes one for the stratiform area time tendency, with the convective mass flux convergence term following Tiedtke (1993), Teixeira (2001) and follow-ons, and the decay term mimicking Hagos et al. (2020), although it is important to note that these terms were used in studies that were prognosing grid-box or fixed-domain stratiform *cloud fraction* or area changes whereas Eq. (1) prognoses *cloud physical area* changes following Lagrangian-tracked MCSs. Hagos et al. (2020) is further similar in that radar data (off the coast of Darwin, Australia) are used to develop a simple analytical model of stratiform area, though individual MCSs were not explicitly tracked in that analysis and the source terms vary in structure.

3.2.1 Constraining the Eq. (1) source term for convective area ($A_{c,SRC}$)

A_c at any given time is estimated by GPM though the time tendency is not, owing to the long GPM orbit re-visit period. However, it is likely unreasonable to assume that A_c is constant over the 30-minute TOOCAN database time step. Our goal is not to develop a new A_c parameterization (a topic worthy of a separate manuscript); we are merely aiming to isolate and

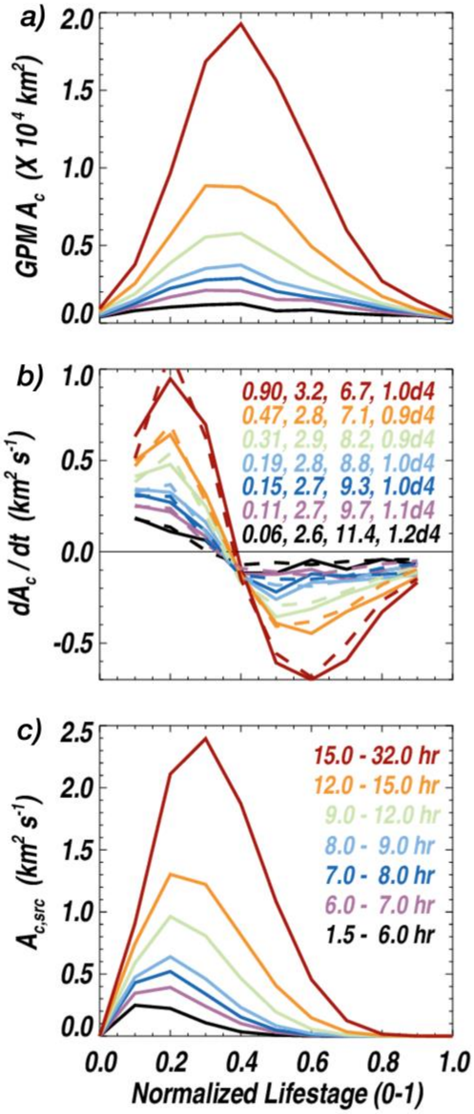

quantify the contribution to total cloud area by new convection area so that we can better describe the growth and decay rates of the stratiform cloud shield given the current state of convective towers. We proceed with a compositing technique to determine $A_{c,SRC}$. Analogous to the development of cloud area source – sink model, we assume the time tendency of A_c following the track of an MCS can be approximated as follows:

$$\frac{dA_c}{dt} \approx A_{c,\,\mathrm{SRC}} - \frac{A_c}{\tau_{\mathrm{cs}}}, \tag{2}$$

where τ_{cs} is the timescale for transition of convective cells to stratiform cells. A term representing evaporation of convective cells without a transition to stratiform is considered negligible within the moist MCS cloud envelope, though such a process could be inevitably wrapped into the computation of τ_{cs}. The average GPM A_c, plotted as a function of normalized life stage, is shown in Fig. 8a for varying system duration bins. From this, we can easily compute the composite dA_c/dt (solid lines of Fig. 8b) where dt is computed by multiplying the increment in normalized life stage by the system duration in seconds. We use a beta distribution to represent $A_{c,\,SRC}$, a function conveniently defined on the [0, 1]

Figure 8. (a) Composite GPM convective area A_c as a function of system life stage (normalized by dividing system life stage hour by total duration). The A_c evolution is shown for different system durations (panel c shows duration legend). (b) Composite dA_c/dt as a function of normalized life stage (solid), with fits overplotted (dashed lines). The fit coefficients for the dA_c/dt model are color-coded by duration and provided in the following order: γ (km^{2}s^{-1}), α (unitless), β (unitless), and τ_{cs} (s). (c) The $A_{c,\,\mathrm{SRC}}$ function used in the growth – decay rate model (see manuscript for discussion).

interval that characterizes the normalized life stage range. dA_c/dt can now be written as follows:

$$\frac{dA_c}{dt} \approx \frac{\gamma}{B(\alpha,\beta)} x^{\alpha-1}(1-x)^{\beta-1} - \frac{A_c}{\tau_{\mathrm{cs}}}, \tag{3}$$

where γ is a scaling factor, $B(\alpha,\beta)$ is the beta function with shape parameters ($\alpha,\beta>0$), and x is the normalized life stage. With A_c, $dA_{c.}/dt$ and x being provided from our composite analyses (Fig. 8), we use a Levenberg-Marquardt algorithm to solve for the unknown coefficients (γ, α, β, τ_{cs}). The fits to $dA_{c.}/dt$ are shown in Fig. 8b (dashed lines), with the coefficients also provided. The fits fully reproduce the observed composite $dA_{c.}/dt$. Interestingly, τ_{cs} is nearly invariant across duration bins, with the timescale for conversion of convective cells to stratiform area being ~2.75 hr (coincidentally, this value falls within the deep-to-stratiform timescale range [0.5 – 3 hr] considered in Khouider et al., 2010). System durations of 6 – 10 hr are most common in the TOOCAN database, and for these systems, $A_{c,SRC}$ predicts that convective area is newly generated, early in the lifecycle (Fig. 8c), at a maximum rate of ~ 0.5 km^2 s^{-1}. Over the IR 30-min time step, this implies a generation of new convective area equivalent to a circle of diameter ~ 30 km.

Currently existing convective area A_c is assumed to transition to stratiform area, and a change in the cloud "type" does not result in a change in A. Thus, we must only account for generation of new convective area in Eq. (1), with no need for the second term of Eq. (2), and hence we substitute the computed $A_{c,SRC}$ functions (plotted in Fig. 8c) directly into the first term on the rhs of Eq. (1) to constrain convective area generation over the 30-min time step.

3.2.2 Reformulating and constraining the Eq. (1) vertical mass flux convergence terms

Bony et al. (2016) and Seeley et al. (2019) explored the convective mass flux convergence term (equivalent to net detrainment) as it relates to understanding tropical cloud fraction sources. Using Weather Research and Forecasting (WRF) simulations, Seeley et al. (2019) found that net detrainment did not explain the altitude of peak cloud fraction. However, it is also evident in Seeley et al. (2019) that for cloud fraction profiles above ~10 km, where entrainment is minimal, convective source formulations represented as net or gross detrainment yield similar results. Such altitudes are closer to the IR-observed MCS cloud tops, and thus, a net detrainment formulation for the convective source term in our analysis is reasonable. The detrainment term can be re-cast in terms of Q_1-Q_R, allowing us to assess this formulation globally across the tropics using GPM Q_1-Q_R mapped to MCS shields. For any system, M_c is equivalent to $\rho A_c w$ (where w is the vertical wind speed averaged over A_c); but, M_c is not observable from GPM since vertical motion is not among those parameters retrieved. From the budget equation for dry static energy ($s = c_pT + gz$, where c_p is the specific heat at constant pressure, T is the temperature, and gz is the geopotential), if we assume small temporal changes in dry static energy (Sobel et al., 2001) across A_c, a small horizontal advection term, and assume convective Q_1-Q_R dominates over radiative heating within the convective cells, we can approximate w as follows:

$$w \approx \left(\frac{1}{c_p}\frac{ds}{dz}\right)^{-1}(Q_1\text{-}Q_{R_{\text{Conv}}}) = \left(\frac{1}{\Gamma-\Gamma_d}\right)(Q_1\text{-}Q_{R_{\text{Conv}}}), \tag{4}$$

where Γ is the average temperature lapse rate across A_c (and subscript d on Γ denotes the dry adiabatic lapse rate) and Q_1-Q_R is in units of K s^{-1}. A_c profiles are not provided by GPM (i.e., convective classification is independent of height) yet a spectrum of convective cells of varying vertical depths likely exists across A_c. Thus, as altitude increases and convective area fraction systematically decreases (Kumar et al., 2015; Giangrande et al., 2016), w computed here might best be thought of as an approximate vertical motion across A_c that likely includes increasing contribution from non-convective motions above the tops of shallower or upward growing convective towers (as opposed to w representing convective core vertical updraft speeds at all altitudes, specifically). With Eq. (4), the second term on the rhs of Eq. (1) can now be approximated as follows:

$$-\frac{1}{\rho}\frac{dM_c}{dz} \approx -\frac{A_c}{\rho}\frac{d}{dz}\left(\rho\frac{Q_1\text{-}Q_{R_{\text{Conv}}}}{\Gamma-\Gamma_d}\right). \tag{5}$$

The third term on the rhs of Eq. (1) can be written like Eq. (5), except with A_c and convective Q_1-Q_R being swapped for the stratiform counterparts. We explore inclusion of this third term in Eq. (1) since the mesoscale divergence near the tops of well-developed precipitating stratiform regions might be significant enough to force an observable lateral expansion of the entire cloud shield.

We use the satellite retrievals discussed in section 2 to populate the two source terms and plot statistics in Fig. 9. The satellite sounder retrievals of temperature are characteristic of non-cloudy unsaturated tropical environments outside of the tracked systems. Thus, to define Γ at all altitudes within any system cloud shield, we assume the atmosphere is saturated and assume a moist adiabatic lapse rate (hereafter, Γ_m) whose magnitude is set to the climatological AIRS grid box Γ_m closest to the tracked system. Since Γ_m varies strongly with temperature, this gives regionally varying lapse rates. For both the CSH (Fig. 9a,b) and SLH (Fig. 9c,d). products, the convective source terms maximize ~1 – 2 km above the stratiform sources. Because of this, the

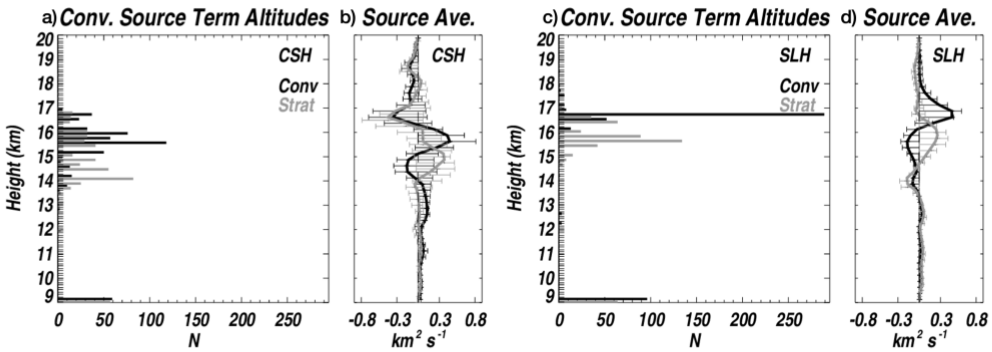

Figure 9. For the CSH product, (a) the height distribution of the maximum value of the cloud area tendency convective source term, and (b) the composite-average source term profile (horizontal lines depict the +/– 1σ range). (c and d): as in a and b, but for the SLH product.

stratiform source terms at lower altitudes would influence the vertical cloud extent and cloud area tendency profile below the cloud top. Thus, the downward-looking two-dimensional GEO-IR satellite perspective will yield a cloud shield tendency largely driven by the convective mass flux term, and so we simplify Eq. (1) further by neglecting the stratiform source term. Fig. 9 suggests large differences in the altitudes of peak cloud area tendencies derived from CSH and SLH. The altitude of the peak source is > 1 km higher in SLH than that inferred from the CSH product. For SLH, the convective and stratiform terms combined suggest a cloud fraction profile that would peak from 16 – 17 km (Fig. 9c,d), which is 1 – 2 km higher than observed (see Seeley et al., 2019). Therefore, in addition to neglecting the stratiform mass flux term, we use the CSH heating product for the remainder of the paper to quantify the magnitude of the convective source term. Additionally, the magnitude of this convective mass flux term is set to the profile maximum above 9 km (i.e., at or above the IR-identified altitude for cold "cloud shield" coverage) in the following analyses.

3.2.3 Final discretized equation for predicting the cloud shield area growth and decay rates.

Regarding the final term of Eq. (1) (the sink term, the last term on the rhs), dissipation of cloud area *A* depends on total ice condensate within cloud. GPM products do not provide all ice condensate species (not to mention the difficulty that exists in retrieving cloud ice accurately (Duncan and Eriksson, 2018)). Sources of ice include convective ice detrainment and saturated ascent in the stratiform/anvil region, with sinks being driven by precipitation. Convective and stratiform latent heating and precipitation terms could be used to partially infer ice condensate if the evolution of these terms along system paths were known; however, GPM provides these estimates at one instant, and though GPM estimates could constrain the current perturbation to total ice condensate within cloud, total ice condensate itself is not. Additionally, since evaporation is slow and inefficient in the cold upper troposphere (Seeley et al., 2019), mixing near cloud edges may actually act to increase cloud area if the ice condensate amount near cloud edges is large enough. These processes are all wrapped into the decay timescale τ of the Eq. (1) sink term.

With $A_{c,SRC}$ now constrained (section 3.2.1) and with reformulation of the convective mass flux term (section 3.2.2), we re-cast the cloud shield area time tendency Eq. (1) as a regression equation with the terms discretized as follows:

$$\frac{\Delta A}{\Delta t} = A_{c,\,\mathrm{SRC}} - C_1 A_c \times max\left[\frac{1}{\rho}\frac{\Delta}{\Delta z}\left(\rho\,\frac{Q_I\text{-}Q_{R_{\mathrm{Conv}}}}{\Gamma_m - \Gamma_d}\right)\right] - C_2\, A, \tag{6}$$

where $\Delta A/\Delta t$ is explicitly provided by TOOCAN (Δt = 30 min), C_1 accounts for possible satellite retrieval limitations in quantifying the vertical profile of convective area and in-cloud lapse rates, C_2 is equal to τ^{-1}, and *max*[…] refers to a search of the maximum of the enclosed term above 9km, as discussed in 3.2.2. We apply Eq. (6) to MCS data binned by convective system duration and *A* time tendencies, solve for C_1 and C_2, and evaluate the model *A* time tendencies. The *A* time tendency bin widths (~ 0.15 $km^2\ s^{-1}$) are chosen so that compositing artifacts are minimized while ensuring each bin has at least one GPM sample. We apply the model to all data combined, and to data in different duration bins separately (using the same bins shown in Fig. 8c) in large part to test the robustness of the model across different system types and subsets of data.

3.3 Growth and decay rates stratified by surface type, system duration and convective organization

The observed and model-predicted dA/dt are shown in Fig. 10 for storms of varying durations (the results for all data combined, independent of duration, is shown in Fig. 12a). Fig. 10 points are coded according to whether the system was over ocean (circles) or land (pluses) and colored according to R_{PA}. The fact that most points fall close to the 1:1 line suggests that the functional form of the cloud shield model is skillful across the spectrum of convective system duration bins and aggregation states. Interestingly, the computed regression coefficients (C_1 and C_2) are largely duration independent, with C_1 ~ 1 and C_2 ~ 0.00018 s^{-1}. That C_1 is nearly unity for each duration bin suggests that the mass flux convergence source term formulated in terms of diabatic heating and moist adiabatic lapse rates is a good approximation, with C_1 not needed. With C_2 having units of s^{-1}, this implies that the IR cloud shield decay timescale is 1 – 2 hr. Seeley et

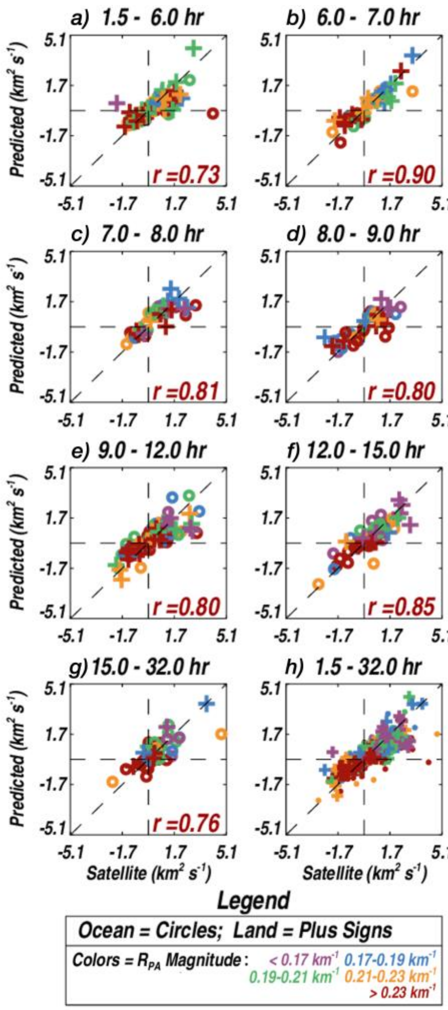

al. (2019) using model simulation experiments derived global ice cloud lifetimes of ~ 5 – 10 hr at 10 – 15 km, with a decrease in the lifetime as altitude increases further, while Hagos et al. (2020) derived a decay timescale of 7 hr for stratiform areas. These decay timescales were computed for convection in aggregate or global cloud analyses as opposed to tracked MCS, and thus the timescale are not apples-to-apples comparable. Since the MCS cloud shields tracked in TOOCAN are likely raining at rates larger than average convective scenes, one might expect that the decay timescales are shorter since precipitation could be a stronger sink of stratiform cloud area.

Fig. 10 does not suggest a larger systematic deviation from the 1:1 line in the predictions for systems over land relative to those over ocean. As mentioned in section 3.1, convection is known to be more intense over land than ocean. The Eq. (5) convective source term yields a source magnitude that peaks near 16.5 km over land and 15.5 km over ocean,

Figure 10. Predicted *dA/dt* versus satellite estimated *dA/dt* for different convective system duration bins, with the plot symbol denoting surface type (ocean = circles, land = plus signs) and symbol color denoting the R_{PA} magnitudes. Correlation coefficients for the prediction vs. observation are shown at the bottom of each panel. The last duration range panel shows all points combined for additional visual comparison across all duration bins.

with the source itself a factor of ~2.5 stronger over land than ocean on average (0.8 km^2 s^{-1} and 2.0 km^2 s^{-1} for ocean and land, respectively). These results are consistent with land – ocean differences in convection, with the increased land source attributed to stronger diabatic heating and a larger vertical gradient in diabatic heating instead of being attributed to moist adiabatic lapse rate differences (not shown). Additionally, departures in the prediction from the 1:1 line do not seem to be dependent on cell aggregation (i.e., R_{PA}). This result is interesting, particularly in light of Hagos et al. (2020) where it was found that if there were more convective cells for a given convective area, growth of the stratiform area was larger. The Hagos et al. (2020) result was interpreted within the context of the "particle fountain" idea proposed by Yuter and Houze (1995), where if convective cells were more scattered like trees in a forest, their ice particles were more likely to fall outside of the existing convective area, thus favoring growth of stratiform cloud regions. For a given convective area, as the number of convective cells increases, the sum of the perimeters surrounding convective cells increases (Fig. 7); therefore, growth of the stratiform region (or cloud shield area in this study, given the correlation with stratiform area) should be larger as R_{PA} increases. Since the source – sink model does not specifically consider convective perimeters, the lack of outliers in the prediction might be surprising.

We investigate this further in Fig. 11a, where the convective source term (i.e., Eq. 5) is plotted as a joint function of convective area A_c and R_{PA}. R_{PA} is one way to quantify convective aggregation, but this metric is also strongly correlated with an independent convective "organization" metric (i.e., the Radar Organization Metric or ROME; Fig. 11f) following Retsch et al. (2020) which specifically defines organization based on the size and proximity of convective cells. As defined here, organization increases as ROME

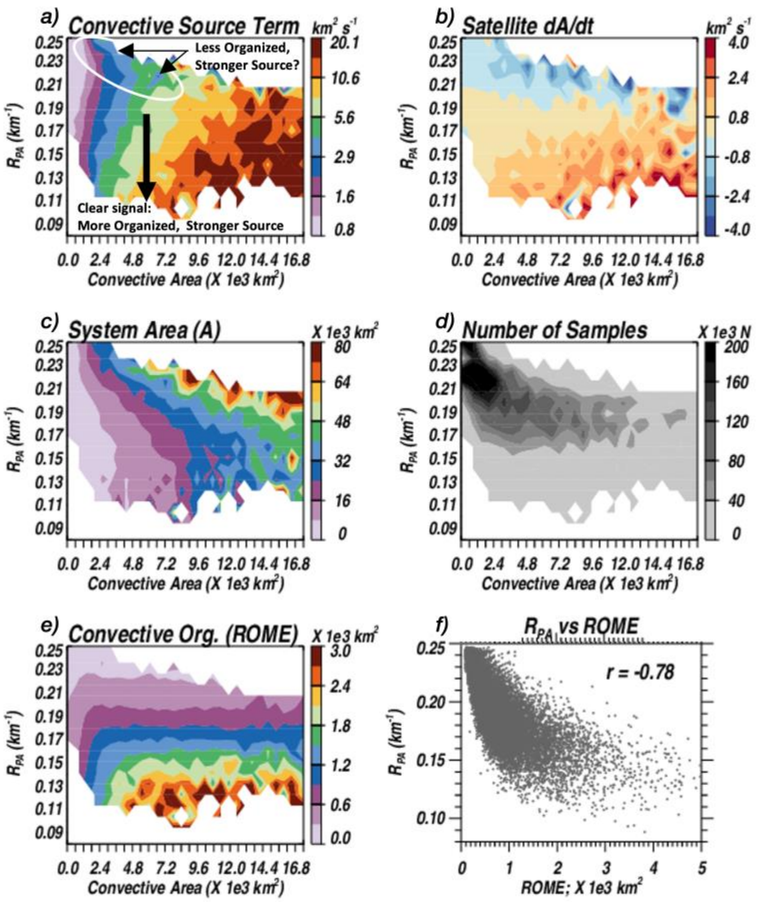

Figure 11. (Left column) From top to bottom, the average convective source term (Eq. 3 in manuscript), average convective system IR-estimated cloud shield area, and average organization of convective cells (defined using the Radar Organization Metric, or ROME, as in Retsch et al. 2020) as a joint function of total convective area (A_c) and the ratio of the sum of convective cell perimeters divided by total convective area (R_{PA}). (Right column) As in left, but for (b) satellite estimated system area time tendency (dA/dt) and (d) number of samples contributing to composites. Panel f illustrates the relationship between R_{PA} and a convective organization diagnostic (ROME).

increases, with the upper limit of organization being equivalent to the mean convective cell area multiplied by 2. Fig. 11e shows how ROME increases as R_{PA} decreases for the same convective area. As expected, Fig. 11a shows that the convective source term increases as A_c increases (and, indeed, the total satellite cloud shield time tendency in Fig. 11b follows this pattern). Additionally, there is a very clear pattern showing an increase in the convective source term as R_{PA} decreases. Interestingly, this tendency reverses when the cloud shield area is undergoing decay on average. In this state, as R_{PA} increases (i.e., organization decreases), the source term also increases (top left portion of Fig. 11a). The latter result is similar to the findings of Hagos et al. (2020). Might this imply that less organized convection during the later decaying stages of system lifecycles favors cloud shield sustenance and increased longevity? At first glance, this seems to be a small portion of the data state space; however, this region of the state space comprises large cloud shield areas and system counts (roughly 20-25% of the data lie above the white-outlined area in the top left panel of Fig. 11). In summary, even though Eq. (6) does not specifically consider convective cell aggregation, there is a signal in the vertical (associated with the convective cell-ensemble Q_1-Q_R height derivative) that is serving as a strong enough proxy to modulate variations in the cloud area source as convective cell organization changes, which is probably why Fig. 10 shows no clear biases in the prediction as cell aggregation varies.

With $A_{c,SRC}$ moved to the lhs of Eq. (6), an anvil cloud shield growth rate equation can be developed (the full anvil is not captured, of course, since the thinner parts of the anvil are likely not detected in the TOOCAN database). Though necessary for development here, in a climate model, $A_{c,SRC}$ would be irrelevant, with convective area being determined by the model's own convective parameterization. Thus, in a model, anvil area growth rate could be predicted based on the convective diabatic heating structure, model A_c, temperature lapse rates, and use of C_2 as derived here (where C_2 can be a fixed, based on results presented, though the processes that govern its magnitude requires additional investigation). It is obvious that in order for the anvil growth rate to be ≥ 0 (i.e, the stratiform/anvil area is sustained or growing), term 2 must be $\geq$ term 3 on the rhs of Eq. (6). If we re-arrange these terms, set C_1 to unity (as discussed), and solve for the convective area fraction necessary for stratiform anvil sustenance, we arrive at the following equation:

$$\frac{A_c}{A} \geq C_2 \,/\, max\left[\frac{1}{\rho}\frac{\Delta}{\Delta z}\left(\rho\frac{Q_1\text{-}Q_{R_{\mathrm{Conv}}}}{\Gamma-\Gamma_d}\right)\right], \qquad (7)$$

where all parameters have been previously introduced. With C_2 fixed at 0.00018 s^{-1}, an analysis of the *max*[…] term (considering all data combined across durations) suggests the convective area fraction must exceed ~ 0.2 in order for the stratiform component of the shield to grow, with the growth rate magnitude itself dependent on A_c and the vertical gradient of diabatic heating and lapse rates.

3.4 Sensitivity of source – sink model to structure and assumptions

Developing a suitable equation for $A_{c,SRC}$ is necessary for determining the structure and coefficients that drive cloud area expansion, though $A_{c,SRC}$ itself, by design, is largely empirical. This is because our focus is on how stratiform anvil areas change given the current structure of convection in a given system, and not on what drives changes in the convective cores themselves. We have tested different functions for deriving $A_{c,SRC}$. Most perform poorly when compared to the GPM A_c composites (Fig. 8a), and that is because few functions can reproduce the beta distribution shape that allows for capturing the sharp increase in A_c production during system growth, quick decay toward the middle life stages, and no production of A_c during later life stages. Originally, we did assume a constant (or 'average') $A_{c,SRC}$, but this led to C_1 and C_2 varying with system duration (though the averages of those two coefficients across all durations were close to the estimates found here). We attribute the variation due to systematic differences in sampling of life stages across system durations. For the shorter-lived (smaller) systems, the GPM swath width often permits a view of systems at random life stages; for the longer-lived (larger) systems, there is a skewing towards earlier life stages since the largest systems reach peak size later, and their expansive cloud shields by then are under sampled by GPM (and not included in our analyses). Since $A_{c,SRC}$ peaks during early stages (Fig. 8c), assuming a constant $A_{c,SRC}$ across the entire lifecycle underestimates the production occurring during early stages often-sampled for longer-lived systems, whereas for the shorter systems, assuming a constant $A_{c,SRC}$ leads to a better result since the underestimation of A_c production earlier is cancelled by the overestimation later. This systematic shift in $A_{c,SRC}$ estimation is compensated by a corresponding systematic change in C_1 and C_2 as system duration increases.

The above discussion motivates the following question: how do our GPM sampling requirements influence our quantitative results? Over 90% of the time when the predicted minus satellite estimated differences exceed 1 km^2 s^{-1}, the MCS cloud shield area was under-sampled by GPM. As mentioned in section 2.1, at least 2/3 of the convective system cloud shield area must be sampled by GPM in order for the data point to be included in development and analysis of the analytical model. Convection occupies a small fraction of a cloud shield, and therefore, it is easy for GPM to completely miss convective cores. This limitation is not resolved by simply increasing the size of our database. Instead, this is the result of system sizes often exceeding the swath width of the GPM DPR orbit, and no sample size will ever permit 2/3 sampling of large MCS shields (Nesbitt et al., 2006; Fiolleau and Roca, 2013b).

While decreasing the 2/3 coverage threshold drastically increases the sample count, there is a price to pay. If convection is missed too often, the convective mass flux source term is artificially zero too frequently. This issue does not simply lead to more scatter in any one duration bin. Instead, with a weaker (or zero) source term, a weaker sink term would also be computed to achieve the best fit to the ensemble of points, and subsequently, the sensitivity of the prediction is lower. This is depicted as a "flattening" in the prediction. Conversely, a more conservative threshold (e.g., 90% coverage), while increasing the probability that convective cores are sampled, results in almost no data being available no matter the record length (and for systems that are sampled, their sizes are often small, since smaller shields are the ones entirely viewable by GPM). Thus, the 2/3 threshold strikes a balance between data samples and system sizes, and the necessity of sampling the convective source. To assess the under-sampling issue further, one fit is re-computed independent of duration bin (Fig. 12a), which clearly resembles all results in the Fig. 10 panels, while another fit

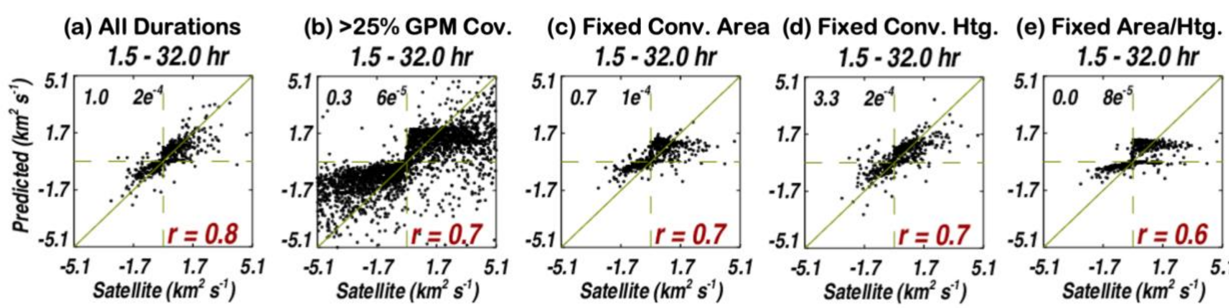

Figure 12. Like Fig. 10, except with varying thresholds used for constraining the convective source term in the cloud shield area time tendency equation and no coding of points based on surface type (land, ocean) or convective organization. From L to R: (a) fits calculated independent of duration bin; (b) calculations performed with less stringent GPM coverage required (>25% of the system shield must be sampled); (c) calculations performed while fixing the convective area to the average across all systems; (d) calculations performed while fixing the convective heating profile to the average across all systems; and, (e) calculations performed while fixing both convective area and convective heating profiles to the average across all systems. For each panel, the C_1 and C_2 coefficients determined from the model fitting are plotted (see manuscript for further discussion).

is recomputed after requiring only 25% of the area to be covered by GPM (Fig. 12b). Clearly, the relationship is not as strong with less sampling of the convective structures, and both growth and decay rates are further underestimated, with a flattening in the prediction observed.

Is the vertical convective heating structure or convective area the key component driving the convective mass flux source term? As a test for system convective core similarity, we swap the mean convective area across all systems for the actual observed convective area and re-compute the fit. Note the poorer fit for this experiment in Fig.12c, particularly when the satellite data indicates the systems are growing. In Fig. 12d, the all-system-average convective heating profile is substituted in, and Fig. 12e shows the results when there is no variation in convection across systems (i.e., mean convective area and mean heating profile are used). That Fig. 12d looks like Fig. 12a suggests that capturing the convective area, via sampling of a large-enough fraction of the system, is most important. In the Fig. 12d experiment, C_1 (though previously equal to 1) becomes a scale factor on convective area (whose magnitude was already influenced by the average vertical derivative of Q_1-Q_R and temperature lapse rates in this experiment). Importantly, Fig. 12d suggests that one could simply use some constant times A_c as the source term of the model, and never consider information about Q_1-Q_R nor temperature lapse rates as we have. In such a case, the computed C_1 coefficient would be ~0.0008 s^{-1}. Of course, the following question would then arise: where does the arbitrary 0.0008 s^{-1} derive from? Clearly then, the advantage of using the convective mass flux source term (Eq (6), second term on rhs) as we have formulated it, instead of some constant multiplied by A_c in a new source term, is that it provides an understanding of the source term physics that clearly tie to the vertical gradient of convective diabatic heating in systems, co-incident with an increasingly stable upper troposphere, which act as pre-factor for determining the quantitative role that convective area plays in cloud shield growth rates.

4 Conclusion

How tropical anvil areal extent will change and modulate radiation as the climate warms is one of the largest uncertainties in recent cloud feedback assessments (e.g., Sherwood et al., 2020), and improved understanding of the spectrum of deep convective system areal extents, how system areas couple with convective and stratiform diabatic heating, and the construction of simple models that can inform GCM convective parameterization is needed. In this work, we specifically focused on increasing our understanding of MCS cloud shield area time tendencies and relationship with convective heating.

Composite analyses show that longer-lived (and larger) deep convective system cloud shields are associated with increased diabatic heating above the melting level (Figs. 2 and 3), largely due to stratiform region heating. The system evolution composites are not necessarily representative of individual system evolutions, though (e.g., Fig. 4). Instead, evolutions may be best thought of as collections of instantaneous bursts in growth mixed with sequences of decay, such that a longer-lived duration may arise from a fortunate series of growth sequences. Results suggest that the growth of a convective system shield is strongly related to generation of convective area and a strong vertical gradient of convective-region heating (computed from its peak above the melting level to the cloud top) forcing lateral cloud growth (Fig. 5). Decay rates are strongly related to the instantaneous size of the cloud shield itself, but exhibit no clear dependence on relative humidity.

A simple convective-source, slow-decay model (Eqs. 1 and 6) informed by the observational results is developed. Since satellite-estimated vertical winds in convection are not available for developing the cloud shield model source term, the model is re-formulated in terms of diabatic heating, an advantage that permits analyses via use of GPM retrieved diabatic heating mapped to MCSs (and which has an analog in GCM output since most convective parameterizations yield diabatic heating profiles). The remaining model terms are quantified using satellite retrievals from GEO-IR, AIRS/MLS and convective area estimates from GPM, and uncertain or unknown coefficients are derived by applying the model to all tropical (land and ocean) scenes and duration bins. The simple cloud shield model often explains over 60% of the 30-min changes in cloud shield areas across the global tropics (with comparable skill across MCS duration bins, and no clear biases for land or ocean systems nor convective cell aggregation). There is a rich structure in the cloud area source term that varies as a function of convective cell organization, with overall, the source term increasing with convective organization, while for decaying shields characterized by smaller convective area overall, the source term sometimes increases as organization decreases. Results further suggest that convective and stratiform rainfall and associated diabatic heating are often coupled, stratiform heating is present at all system life stages past initiation (Fig. 3), and stratiform area is continually produced along the path of the MCS (Eq. 1). Thus, the “convective to stratiform transition” onset period might also be considered an emergent property, useful for evaluating output from a GCM at the grid box and timestep-scales during parameterization development, as opposed to a process that happens abruptly or at a fixed life stage.

Toward understanding the distribution of convective system durations, work is underway to understand factors favoring convective area maintenance and/or re-generation following the path of a system so as to understand the functional form of $A_{c,SRC}$ and to understand its variation across systems of varying duration. Extending the Lagrangian analyses to three-dimensional MCS cloud volumes via analyses of height-resolved cloud fractions alongside the stratiform area source term, exploring the role of radiative heating (Gasparini et al., 2019) in cloud shield time tendencies, and understanding how stratiform precipitation sinks, vertical wind shear, and organization metrics conspire to set the magnitude of the cloud shield decay term timescale τ are other avenues being pursued. An overall objective is to provide improved process-level understanding and useful observational depictions for improving the representation of convection in parameterized GCMs tasked with providing projections of 21st century climate, the reliability of which depends on accurately representing the spectrum of cloud feedbacks (Hartmann and Larson, 2002; Zelinka and Hartmann, 2010, 2011; Bony et al., 2015), including the role of organized convection (Moncrieff, 2019) and convection-driven high cloudiness.

Acknowledgements

Computing resources for data analysis were provided by the NASA High-End Computing (HEC) Program through the NASA Center for Climate Simulation (NCCS) at the Goddard Space Flight Center. This research was supported by the Precipitation Measurement Missions program (RTOP WBS #573945.04.18.03.60), the Terra, Aqua, and Suomi NPP program (Grants #80NSSC18K1030 and #80NSSC21K1978), and the NASA Data for Operation and Assessment program (Grant #NNX17AF46G). All data used for analysis and analytical model development are available in the public domain. The TOOCAN convective system tracking database is available at https://toocan.ipsl.fr/toocandatabase/. The GPM CSH and SLH Q_1-Q_R, rainfall and convective-stratiform pixel identification are available from NASA's Goddard Earth Sciences Data and Information Services Center (GES DISC) at https://gpm1.gesdisc.eosdis.nasa.gov/data/GPM_L2/, while AIRS V6 water vapor Level 2 data mapped to MCSs are available from GES DISC at https://disc.gsfc.nasa.gov/datasets/AIRS2RET_006/summary/. AIRS V6 and MLS V3 gridded (Level 3) datasets used for computation of climatological moist adiabatic lapse rates are available from the Observations for Model Intercomparison Project (Obs4MIPS) archive hosted on the Earth System Grid Federation at https://esgf-node.llnl.gov/projects/obs4mips/SatelliteDataProducts. We thank Niki Barolini for the design of Figure 7. Helpful comments by external referees provided on an earlier manuscript submitted for review are acknowledged, and we thank Prof. Courtney Schumacher and two anonymous reviewers for their comments and constructive feedback, which improved this manuscript.

REFERENCES

Bony, S., B. Stevens, D.M.W. Frierson, C. Jakob, M. Kageyama, R. Pincus, T.G. Shepherd, S.C. Sherwood, A.P. Siebesma, A.H. Sobel, M. Watanabe, and M.J. Webb, 2015: Clouds, circulation and climate sensitivity. *Nature Geosci.*, **8**, 261-268.

Bony, S., B. Stevens, D. Coppin, T. Becker, K.A. Reed, A. Voigt, and B. Medeiros, 2016: Thermodynamic control of anvil cloud amount. *Proc. Nat. Acad. Sci.*, **113**, 8927-8932.

Bouniol, D., R. Roca, T. Fiolleau, and D. E. Poan, 2016: Macrophysical, Microphysical, and Radiative Properties of Tropical Mesoscale Convective Systems over Their Life Cycle. *J. Clim.*, **29**, 3353–3371.

Chahine, M. T., et al., 2006: AIRS: Improving weather forecasting and providing new data on greenhouse gases. *Bull. Amer. Meteor. Soc.*, **87**, 911–926.

Duncan, D.I., C.D. Kummerow, and G.S. Elsaesser, 2014: A Lagrangian analysis of deep convective systems and their local environmental effects. *J. Clim.*, **27**, 2072-2086.

Duncan, D.I., and P. Eriksson, 2018: An update on global atmospheric ice estimates from satellite observations and reanalyses. *Atmos. Chem. Phys.*, **18**, 11205-11219.

Elsaesser, G.S., C.D. Kummerow, T.S. L'Ecuyer, Y.N. Takayabu, and S. Shige, 2010: Observed self-similarity of precipitation regimes over the tropical oceans. *J. Clim.*, **23**, 2686-2698.

Elsaesser, G.S., and C.D. Kummerow, 2013: A multisensor observational depiction of the transition from light to heavy rainfall on subdaily time scales. *J. Atmos. Sci.*, **70**, 2309-2324.

Elsaesser, G.S., A.D. Del Genio, J. Jiang, and M. van Lier-Walqui, 2017: An improved convective ice parameterization for the NASA GISS Global Climate Model and impacts on cloud ice simulation. *J. Clim.*, **30**, 317-336.

Feng, Z., X. Dong, B. Xi, S. A. McFarlane, A. Kennedy, B. Lin, and P. Minnis, 2012: Life cycle of midlatitude deep convective systems in a Lagrangian framework, *J. Geophys. Res.*, **117**, D23201, doi:10.1029/2012JD018362.

Feng, Z., L. R. Leung, R. A. Houze, S. Hagos, J. Hardin, Q. Yang, Q., et al., 2018: Structure and evolution of mesoscale convective systems: Sensitivity to cloud microphysics in convection-permitting simulations over the United States. *JAMES*, **10**, 1470–1494.

Feng, Z., R. A. Houze, L. R. Leung, F. Song, J. C. Hardin, J. Wang, W. I. Gustafson, and C. R. Homeyer, 2019: Spatiotemporal Characteristics and Large-Scale Environments of Mesoscale Convective Systems East of the Rocky Mountains. *J. Clim.*, **32**, 7303–7328.

Feng, Z., F. Song, K. Sakaguchi, and L. R. Leung, 2021: Evaluation of Mesoscale Convective Systems in Climate Simulations: Methodological Development and Results from MPAS-CAM over the United States. *J. Clim.*, **34**, 2611–2633.

Fiolleau, T., and R. Roca, 2013a: An algorithm for the detection and tracking of tropical mesoscale convective systems using infrared images from geostationary satellite. *IEEE Trans. Geosci. Remote Sens.*, **51**, 4302-4315.

Fiolleau, T., and R. Roca, 2013b: Composite life cycle of tropical mesoscale convective systems from geostationary and low Earth orbit satellite observations: method and sampling considerations. *Q. J. R. Meteorol. Soc.*, **139**, 941-953.

Fiolleau, T., R. Roca, S. Cloché, D. Bouniol, P. Raberanto, 2020: Homogenization of geostationary infrared imager channels for cold cloud studies using Megha-Tropiques/ScaRaB. *IEEE Trans. Geosci. Remote Sens.*, **58**, 6609-6622.

Futyan, J., and A. D. Del Genio, 2007: Deep convective system evolution over Africa and the tropical Atlantic. *J. Clim.*, **20**, 5041-5060.

Gasparini B., P. N. Blossey, D. L. Hartmann, G. Lin, and J. Fan, 2019: What drives the life cycle of tropical anvil clouds? *JAMES*, **11**, 2586–2605. https://doi. org/10.1029/2019MS001736.

Giangrande, S. E., T. Toto, M. P. Jensen, M. J. Bartholomew, Z. Feng, A. Protat, C. R. Williams, C. Schumacher, and L. Machado, 2016: Convective cloud vertical velocity and mass-flux characteristics from radar wind profiler observations during GoAmazon2014/5. *J. Geophys. Res. Atmos.*, **121**, 12891–12913.

Grecu, M., W.S. Olson, S.J. Munchak, S. Ringerud, L.Liao, Z.S. Haddad, B.L. Kelley, and S.F. McLaughlin, 2016: The GPM combined algorithm. *J. Atmos. Ocean. Tech.*, **33**, 2225-2245.

Hagos, S., Z. Feng, S. McFarlane, and L. R. Leung, 2013: Environment and the Lifetime of Tropical Deep Convection in a Cloud-Permitting Regional Model Simulation. *J. Atmos. Sci.*, **70**, 2409–2425.

Hagos, S., Z. Feng, R. S. Plant, and A. Protat, 2020: A machine learning assisted development of a model for the populations of convective and stratiform clouds. *JAMES*, **12**, doi: 10.1029/2019MS001798.

Hannah, W.M., B.E. Mapes, and G.S. Elsaesser, 2016: A Lagrangian view of moisture dynamics during DYNAMO. *J. Atmos. Sci.*, **73**, 1967-1985.

Hartmann, D.L., H.H. Hendon, and R.A. Houze Jr., 1984: Some implications of the mesoscale circulations in tropical cloud clusters for large-scale dynamics and climate. *J. Atmos. Sci.*, **41**, 113-121.

Hartmann, D.L., and K. Larson, 2002: An important constraint on tropical cloud-climate feedback. *Geophys. Res. Letters*, **29**, 1951, doi:10.1029/2002GL015835.

Holloway, C.E., A.A. Wing, S. Bony, C. Muller, H. Masunaga, T.S. L'Ecuyer, D.D. Turner, and P. Zuidema, 2017: Observing convective aggregation. *Surv. Geophys.*, **38**, 1199-1236.

Houze, R. A. Jr., 1989: Observed structure of mesoscale convective systems and implications for large scale heating. *Quart. J. R. Meteor. Soc.*, **115**, 425– 461.

Houze, R. A. Jr., 1997: Stratiform Precipitation in Regions of Convection: A Meteorological Paradox? *Bull. Amer. Meteor. Soc.*, **78**, 2179–2196.

Houze, R. A., 2004: Mesoscale convective systems. *Rev. Geophys*. **42**, 1–43.

Iguchi, T., S. Seto, et al., 2012: An overview of the precipitation retrieval algorithm for the Dual-frequency Precipitation Radar (DPR) on the Global Precipitation Measurement (GPM) mission's core satellite. https://doi.org/10.1117/12.976823.

Inoue, K., and L. Back, 2015: Column-Integrated Moist Static Energy Budget Analysis on Various Time Scales during TOGA COARE, *J. Atmos. Sci*, **72**, 1856-1871.

Khouider, B., J. Biello, and A. J. Majda, 2010: A Stochastic Multicloud Model for Tropical Convection. *Commun. Math. Sci.*, **8**, 187–216.

Kiladis, G. N., K. H. Straub, and P. T. Haertel, 2005: Zonal and vertical structure of the Madden–

Julian oscillation. *J. Atmos. Sci.*, **62**, 2790–2809.

Knapp, K. R., M. C. Kruk, D. H. Levinson, H. J. Diamond, and C. J. Neumann, 2010: The International Best Track Archive for Climate Stewardship (IBTrACS), *Bull. Amer. Meteor. Soc.*, **91**(3), 363-376.

Kumar, V. V., C. Jakob, A. Protat, C. R. Williams, and P. T. May, 2015: Mass-Flux Characteristics of Tropical Cumulus Clouds from Wind Profiler Observations at Darwin, Australia. *J. Atmos. Sci.*, **72**, 1837–1855.

Lang, S.E., and W.-K. Tao, 2018: The next-generation Goddard Convective-Stratiform Heating algorithm: New tropical and warm season retrievals for GPM. *J. Clim.*, **31**, 5997-6026.

Lin, J., B. E. Mapes, M. Zhang, and M. Newman, 2004: Stratiform precipitation, vertical heating profiles, and the Madden–Julian oscillation. *J. Atmos. Sci.*, **61**, 296–309.

Lin, L., Q. Fu, X. Liu, Y. Shan, S.E. Giangrande, G.S. Elsaesser, K. Yang, and D. Wang, 2021: Improved convective ice microphysics parameterization in the NCAR CAM model. *J. Geophys. Res. Atmos.*, **126**, no. 9, e2020JD034157, doi:10.1029/2020JD034157.

Liu, C., E. J. Zipser, D. J. Cecil, S. W. Nesbitt, and S. Sherwood, 2008: A Cloud and Precipitation Feature Database from Nine Years of TRMM Observations. *J. Appl. Meteor. Clim.*, **47**, 2712-2728.

Liu, C., 2011: Rainfall Contributions from Precipitation Systems with Different Sizes, Convective Intensities, and Durations over the Tropics and Subtropics, *J. Hydrometeor.*, **12**, 394-412.

Liu, C., S. Shige, Y. N. Takayabu, and E. Zipser, 2015: Latent Heating Contribution from Precipitation Systems with Different Sizes, Depths, and Intensities in the Tropics, *J. Clim.*, **28**, 186-203.

Lucas, C., E. J. Zipser, and M. A. Lemone, 1994: Vertical velocity in oceanic convection off tropical Australia. *J. Atmos. Sci.*, **51(21)**, 3183-3193.

Machado, L.A.T., W.B. Rossow, R.L. Guedes, and A.W. Walker, 1998: Life cycle variations of mesoscale convective systems over the Americas. *Mon. Wea. Rev.*, **126**, 1630-1654.

Machado, L.A.T, and H. Laurent, 2004: The convective system area expansion over Amazonia and its relationship with convective system life duration and high-level wind divergence.

Mon. Wea. Rev., **132**, 714–725.

Mapes, B., and R. Neale, 2011: Parameterizing convective organization to escape the entrainment dilemma. *JAMES*, **3**, M06004, doi:10.1029/2011MS000042.

Mauritsen, T., and Coauthors, 2012: Tuning the climate of a global model. *J. Adv. Model. Earth Syst.*, **4**, M00A01, doi:10.1029/2012MS000154.

Moncrieff, M.W., C. Liu, and P. Bogenschutz, 2017: Simulation, modeling, and dynamically based parameterization of organized tropical convection for global climate models. *J. Atmos. Sci.*, **74**, 1363-1380.

Moncrieff, M. W., 2019: Toward a Dynamical Foundation for Organized Convection Parameterization in GCMs. *Geophys. Res. Lett.*, **46**, 14103– 14108.

Naud, C.M., A.D. Del Genio, M. Bauer, and W. Kovari, 2010: Cloud vertical distribution across warm and cold fronts in CloudSat-CALIPSO data and a general circulation model. *J. Clim.*, **23**, 3397-3415.

Naud, C. M., J. F. Booth, J. F., and A. D. Del Genio, 2016: The Relationship between Boundary Layer Stability and Cloud Cover in the Post-Cold-Frontal Region, *J. Clim.*, **29**, 8129-8149.

Nesbitt, S. W., R. Cifelli, and S. A. Rutledge, 2006: Storm Morphology and Rainfall Characteristics of TRMM Precipitation Features. *Mon. Weather Rev.*, **134**, 2702–2721.

Parker, M. D., and R. H. Johnson, 2000: Organizational Modes of Midlatitude Mesoscale Convective Systems. *Mon. Wea. Rev.*, **128**, 3413–3436.

Prein, A. F., C. Liu, K. Ikeda, S. B. Tier, R. M. Rasmussen,, G. J. Holland, and M. P. Clark, 2017: Increased rainfall volume from future convective storms in the US. *Nat. Clim. Chang.*, **7**, 880–884.

Rapp, A.D., G. Elsaesser, and C. Kummerow, 2009: A combined multisensor optimal estimation retrieval algorithm for oceanic warm rain clouds. *J. Appl. Meteorol. Climatol.*, **48**, 2242-2256.

Retsch, M. H., C. Jakob, and M. S. Singh, 2020: Assessing Convective Organization in Tropical Radar Observations. *J. Geophys. Res.: Atmos.*, **125**, e2019D031801.

Roca, R., J. Aublanc, P. Chambon, T. Fiolleau, and N. Viltard, 2014: Robust Observational

Quantification of the Contribution of Mesoscale Convective Systems to Rainfall in the Tropics. *J. Clim.*, **27**, 4952–4958.

Roca, R., T. Fiolleau, and D. Bouniol, 2017: A simple model of the life cycle of mesoscale convective system cloud shield in the tropics. *J. Clim.*, **30**, 4283-4298.

Roca, R., and T. Fiolleau, 2020: Extreme precipitation in the tropics is closely associated with long-lived convective systems. *Commun. Earth. Environ.* **1,** 18. https://doi.org/10.1038/s43247-020-00015-4.

Schiro, K. A., S. C. Sullivan, Y.-H. Kuo, H. Su, P. Gentine, G. S. Elsaesser, J. H. Jiang, J. D. Neelin, 2020: Environmental controls on tropical mesoscale convective system precipitation intensity. *J. Atmos. Sci.*, **77**, 4233-4249.

Schmidt, G.A., D. Bader, L.J. Donner, G.S. Elsaesser, J.-C. Golaz, C. Hannay, A. Molod, R. Neale, and S. Saha, 2017: Practice and philosophy of climate model tuning across six U.S. modeling centers. *Geosci. Model Dev.*, **10**, 3207-3223, doi:10.5194/gmd-10-3207-2017.

Schneider, T., S. Lan, A. Stewart, and J. Teixeira, 2017: Earth system modeling 2.0: A blueprint for models that learn from observations and targeted high-resolution simulations. *Geophys. Res. Lett.*, **44**, 12396-12417.

Schumacher, C. and R. A. Houze Jr., 2003a: Stratiform rain in the tropics as seen by the TRMM Precipitation Radar. *J. Clim.*, **116**, 1739-1756.

Schumacher, C. and R. A. Houze Jr., 2003b: The TRMM Precipitation Radar's view of shallow, isolated rain. *J. Appl. Meteorol.*, **42**, 1519-1524.

Schumacher, C., R.A. Houze Jr., and I. Kraucunas, 2004: The tropical dynamical response to latent heating estimates derived from the TRMM Precipitation Radar. *J. Atmos. Sci.*, **61**, 1341-1358.

Schumacher, C. and R. A. Houze Jr., 2006: Stratiform precipitation production over sub-Saharan Africa and the tropical East Atlantic as observed by TRMM. *Q.J.R. Meteorol. Soc.*, **132**, 2235-2255.

Seeley, J. T., N. Jeevanjee, W. Langhans, and D. M. Romps, 2019: Formation of tropical anvil clouds by slow evaporation. *Geophys. Res. Lett.*, **46**, https://doi.org/10.1029/2018GL080747.

Sherwood, S. C., M. J. Webb, J. D. Annan, J. D., K. C. Armour, P. M. Forster, J. C. Hargreaves, et al., 2020: An assessment of Earth's climate sensitivity using multiple lines of evidence. *Reviews of Geophysics*, 58, e2019RG000678.

Shige, S., Y.N. Takayabu, S. Kida, W.-K. Tao, X. Zeng, C. Yokoyama, and T. L'Ecuyer, 2009: Spectral retrieval of latent heating profiles from TRMM PR data. Part IV: Comparisons of lookup tables from two- and three-dimensional simulations. *J. Clim.*, **22**, 5577-5594.

Skofronick-Jackson, et al., 2017: The Global Precipitation Measurement (GPM) Mission for Science and Society, *Bull. Amer. Meteor. Soc.*, **98**, 1679-1695.

Sobel, A. H., J. Nilsson, and L. M. Polvani, 2001: The Weak Temperature Gradient Approximation and Balanced Tropical Moisture Waves, *J. Atmos. Sci.*, **58**, 3650-3665.

Takahashi, H., Z. J. Luo, and G. L. Stephens, 2017: Level of neutral buoyancy, deep convective outflow, and convective core: New perspectives based on 5 years of CloudSat data. *J. Geophys. Res.: Atmos.*, **122(5)**, 2958-2969.

Takahashi, H., Z. J. Luo, and G. L. Stephens, 2021: Revisiting the entrainment relationship of convective plumes: A perspective from global observations, *Geophys. Res. Lett.*, https://doi.org/10.1029/2020GL092349.

Tan, J., C. Jakob, W.B. Rossow, and G. Tselioudis, 2015: Increases in tropical rainfall driven by changes in frequency of organized deep convection. *Nature*, **519**, 451-454.

Tao, W.-K., and M. W. Moncrieff, 2009: Multiscale cloud system modeling. *Rev. Geophys.*, 47, RG4002, doi:10.1029/2008RG000276.

Tao, W.-K., and Co-Authors, 2016: TRMM Latent Heating Retrieval: Applications and Comparisons with Field Campaigns and Large-Scale Analyses. *Meteor. Monographs*, 56, 2.1-2.34.

Tao, W.-K., T. Iguchi, and S. Lang, 2019: Expanding the Goddard CSH Algorithm for GPM: New Extratropical Retrievals. *J. Appl. Meteor. Clim.*, 58, 921-946.

Teixeira, J., 2001: Cloud Fraction and Relative Humidity in a Prognostic Cloud Fraction Scheme. *Mon. Wea. Rev.*, **129**, 1750–1753.

Tiedtke, M., 1993: Representation of Clouds in Large-Scale Models. *Mon. Wea. Rev.*, **121**, 3040 - 3061.

Tobin, I., S. Bony, and R. Roca, 2012: Observational evidence for relationships between the degree of aggregation of deep convection, water vapor, surface fluxes, and radiation. *J. Climate*, **25**, 6885-6904.

Tobin, I., S. Bony, C.E. Holloway, J.Y. Grandpeix, G. Seze, D. Coppin, S.J. Woolnough, and R. Roca, 2013: Does convective aggregation need to be represented in cumulus parameterizations? *JAMES,* **5**, 692-703.

Vant-Hull, B., W. Rossow, and C. Pearl, 2016: Global comparisons of regional life cycle properties and motion of multiday convective systems: tropical and midlatitude land and ocean. J. *Clim*. **29**, 5837–5858.

Wang, D., S. E. Giangrande, K. Schiro, M. P. Jensen, and R. A. Houze, 2019: The characteristics of tropical and midlatitude mesoscale convective systems as revealed by radar wind profilers. *J. Geophys. Res. Atmos.*, **124**, 4601– 4619.

Wang, D., S. E. Giangrande, Z. Feng, J. C. Hardin, and A. F. Prein, 2020: Updraft and downdraft core size and intensity as revealed by radar wind profilers: MCS observations and idealized model comparisons. *J. Geophys. Res. Atmos.*, **125**, https://doi.org/10.1029/2019JD031774.

Waters, J. W., et al., 2006: The Earth Observing System Microwave Limb Sounder (EOS MLS) on the Aura Satellite. *IEEE Trans. Geosci. Rem. Sens.*, **44**, 1075-1092.

Yuter, S. E., and R. A. Houze Jr., 1995: Three-dimensional kinematic and microphysical evolution of Florida cumulonimbus. Part III: Vertical mass transport, mass divergence, and synthesis. *Mon. Wea. Rev.,* **123**, 1964-1983.

Yuter, S. E., and R. A. Houze Jr., 1998: The natural variability of precipitating clouds over the western Pacific warm pool. *Q. J. R. Meteorol. Soc.*, **124**, 53-99.

Zelinka, M.D., and D.L. Hartmann, 2010: Why is longwave cloud feedback positive? *J. Geophys. Res.,* **115**, D16117, doi:10.1029/2010JD013817.

Zelinka, M.D., and D.L. Hartmann, 2011: The observed sensitivity of high clouds to mean surface temperature anomalies in the tropics. *J. Geophys. Res.*, **116**, D23103, doi:10.1029/2011JD016549.

Zipser, E. J., and M. A. LeMone, 1980: Cumulonimbus vertical velocity events in GATE. Part II: Synthesis and model core structure. *J. Atmos. Sci.*, **37(11)**, 2458-2469.